



Article

# Self-Normalizing Multi-Omics Neural Network for Pan-Cancer Prognostication

Asim Waqas <sup>1,2,3,\*</sup>, Aakash Tripathi <sup>2,3</sup>, Sabeen Ahmed <sup>2,3</sup>, Ashwin Mukund <sup>2</sup>, Hamza Farooq <sup>4</sup>, Joseph O. Johnson <sup>5</sup>, Paul A. Stewart <sup>6,7</sup>, Mia Naeini <sup>3</sup>, Matthew B. Schabath <sup>1</sup> and Ghulam Rasool <sup>2,3,8,9</sup>

- <sup>1</sup> Department of Cancer Epidemiology, Moffitt Cancer Center and Research Institute, Tampa, FL 33612, USA; matthew.schabath@moffitt.org
  - <sup>2</sup> Department of Machine Learning, Moffitt Cancer Center and Research Institute, Tampa, FL 33612, USA; aakash.tripathi@moffitt.org (A.T.); sabeen.ahmed@moffitt.org (S.A.); ashwin.mukund@moffitt.org (A.M.); ghulam.rasool@moffitt.org (G.R.)
  - <sup>3</sup> Department of Electrical Engineering, University of South Florida, Tampa, FL 33620, USA; mnaeini@usf.edu
  - <sup>4</sup> Center for Magnetic Resonance Research, University of Minnesota, Minneapolis, MN 55455, USA; faroo014@umn.edu
  - <sup>5</sup> Analytic Microscopy Core Facility, Moffitt Cancer Center and Research Institute, Tampa, FL 33612, USA; joseph.johnson@moffitt.org
  - <sup>6</sup> Huntsman Cancer Institute, University of Utah, Salt Lake City, UT 84112, USA; paul.stewart@hci.utah.edu
  - <sup>7</sup> Department of Nutrition and Integrative Physiology, University of Utah, Salt Lake City, UT 84112, USA
  - <sup>8</sup> Department of Neuro-Oncology, Moffitt Cancer Center and Research Institute, Tampa, FL 33612, USA
  - <sup>9</sup> Department of Oncologic Sciences, University of South Florida, Tampa, FL 33612, USA
- \* Correspondence: asim.waqas@moffitt.org  
† These authors contributed equally to this work.

## Abstract

Prognostic markers such as overall survival (OS) and tertiary lymphoid structure (TLS) ratios, alongside diagnostic signatures like primary cancer-type classification, provide critical information for treatment selection, risk stratification, and longitudinal care planning across the oncology continuum. However, extracting these signals solely from sparse, high-dimensional multi-omics data remains a major challenge due to heterogeneity and frequent missingness in patient profiles. To address this challenge, we present SeNMo, a self-normalizing deep neural network trained on five heterogeneous omics layers—gene expression, DNA methylation, miRNA abundance, somatic mutations, and protein expression—along with the clinical variables, that learns a unified representation robust to missing modalities. Trained on more than 10,000 patient profiles across 32 tumor types from The Cancer Genome Atlas (TCGA), SeNMo provides a baseline that can be readily fine-tuned for diverse downstream tasks. On a held-out TCGA test set, the model achieved a concordance index of 0.758 for OS prediction, while external evaluation yielded 0.73 on the CPTAC lung squamous cell carcinoma cohort and 0.66 on an independent 108-patient Moffitt Cancer Center cohort. Furthermore, on Moffitt’s cohort, baseline SeNMo fine-tuned for TLS ratio prediction aligned with expert annotations ( $p < 0.05$ ) and sharply separated high- versus low-TLS groups, reflecting distinct survival outcomes. Without altering the backbone, a single linear head classified primary cancer type with 99.8% accuracy across the 33 classes. By unifying diagnostic and prognostic predictions in a modality-robust architecture, SeNMo demonstrated strong performance across multiple clinically relevant tasks, including survival estimation, cancer classification, and TLS ratio prediction, highlighting its translational potential for multi-omics oncology applications.

**Keywords:** cancer; oncology; multi-omics; multimodal; pan-cancer; machine learning; deep learning; survival; classification



Academic Editor: Apostolos Zaravinos

Received: 19 June 2025

Revised: 23 July 2025

Accepted: 28 July 2025

Published: 30 July 2025

**Citation:** Waqas, A.; Tripathi, A.; Ahmed, S.; Mukund, A.; Farooq, H.; Johnson, J.O.; Stewart, P.A.; Naeini, M.; Schabath, M.B.; Rasool, G. Self-Normalizing Multi-Omics Neural Network for Pan-Cancer Prognostication. *Int. J. Mol. Sci.* **2025**, *26*, 7358. <https://doi.org/10.3390/ijms26157358>

**Copyright:** © 2025 by the authors. Licensee MDPI, Basel, Switzerland. This article is an open access article distributed under the terms and conditions of the Creative Commons Attribution (CC BY) license (<https://creativecommons.org/licenses/by/4.0/>).

## 1. Introduction

Developing accurate prognostic and diagnostic models is central to advancing precision oncology. Multi-omics data, spanning gene expression, DNA methylation, somatic mutations, protein levels, and miRNA abundance, offer unprecedented opportunities to build such models by capturing diverse molecular signals linked to cancer outcomes and phenotypes [1,2]. However, leveraging these high-dimensional data across tumor types remains a major challenge due to frequent missingness, data heterogeneity, and the lack of scalable integration frameworks. Pan-cancer analysis provides a compelling approach to address these challenges by uncovering both shared and distinct molecular patterns across cancers. However, few existing models can robustly integrate multiple omics modalities and generalize to unseen data or tasks. Addressing this gap requires unified architectures that are modality-robust, clinically relevant, and capable of supporting diverse tasks such as survival prediction, tumor classification, and immune microenvironment assessment.

Prognostic and diagnostic models built on molecular data are an important source for informing treatment selection, stratifying risk, and guiding follow-up strategies in oncology. Overall survival (OS) estimation provides a foundational metric for understanding disease trajectory and evaluating therapeutic impact. Accurate classification of the primary cancer type is equally critical, especially for tumors with ambiguous histology or metastatic presentation, where misdiagnosis can lead to suboptimal care. In parallel, the tumor immune microenvironment, reflected in features like tertiary lymphoid structures (TLS), is gaining recognition as a key determinant of immunotherapy response and long-term outcomes. While these clinical endpoints are often studied in isolation, integrating them into a unified modeling framework can support a more comprehensive view of disease biology and prognosis. A pan-cancer, multi-omics approach offers the potential to power such models by leveraging diverse signals from thousands of patients and tumor types.

Despite promising advances in multi-omics modeling, existing approaches are often constrained by narrow scope, limited modality integration, or weak generalization across tumor types and tasks. Many frameworks are trained on a single omics layer or focus on a specific cancer type, limiting their translational relevance in heterogeneous clinical settings. Others rely on complex feature engineering pipelines that may not scale to large datasets or adapt well to missing data. Deep learning models have shown strong performance in specific applications, but are frequently sensitive to modality dropout, overfitting, and lack of task transferability. Moreover, few models are designed to jointly support survival analysis, diagnostic classification, and immune microenvironment characterization in a single architecture. These gaps highlight the need for a unified, pan-cancer framework that can robustly integrate heterogeneous multi-omics data, support multiple clinically relevant tasks, and generalize across datasets without extensive retraining.

To address these challenges, we developed SeNMo—a self-normalizing deep neural network designed to integrate six heterogeneous data modalities, including gene expression, DNA methylation, miRNA abundance, somatic mutations, protein expression, and clinical variables. Trained on over 10,000 patient samples across 33 tumor types from The Cancer Genome Atlas (TCGA), SeNMo learns a unified, low-dimensional representation that is robust to missing modalities and adaptable to multiple downstream tasks. Without altering the backbone architecture, we fine-tuned SeNMo for three clinically meaningful applications: OS prediction, primary cancer type classification, and TLS ratio estimation. The model's self-normalizing architecture enhances training stability across high-dimensional inputs, while its generalizability enables deployment on external datasets with minimal adjustment. Together, these features make SeNMo a versatile tool for multimodal cancer prognostication and diagnostic support. Figure 1 presents the entire outline of this work.

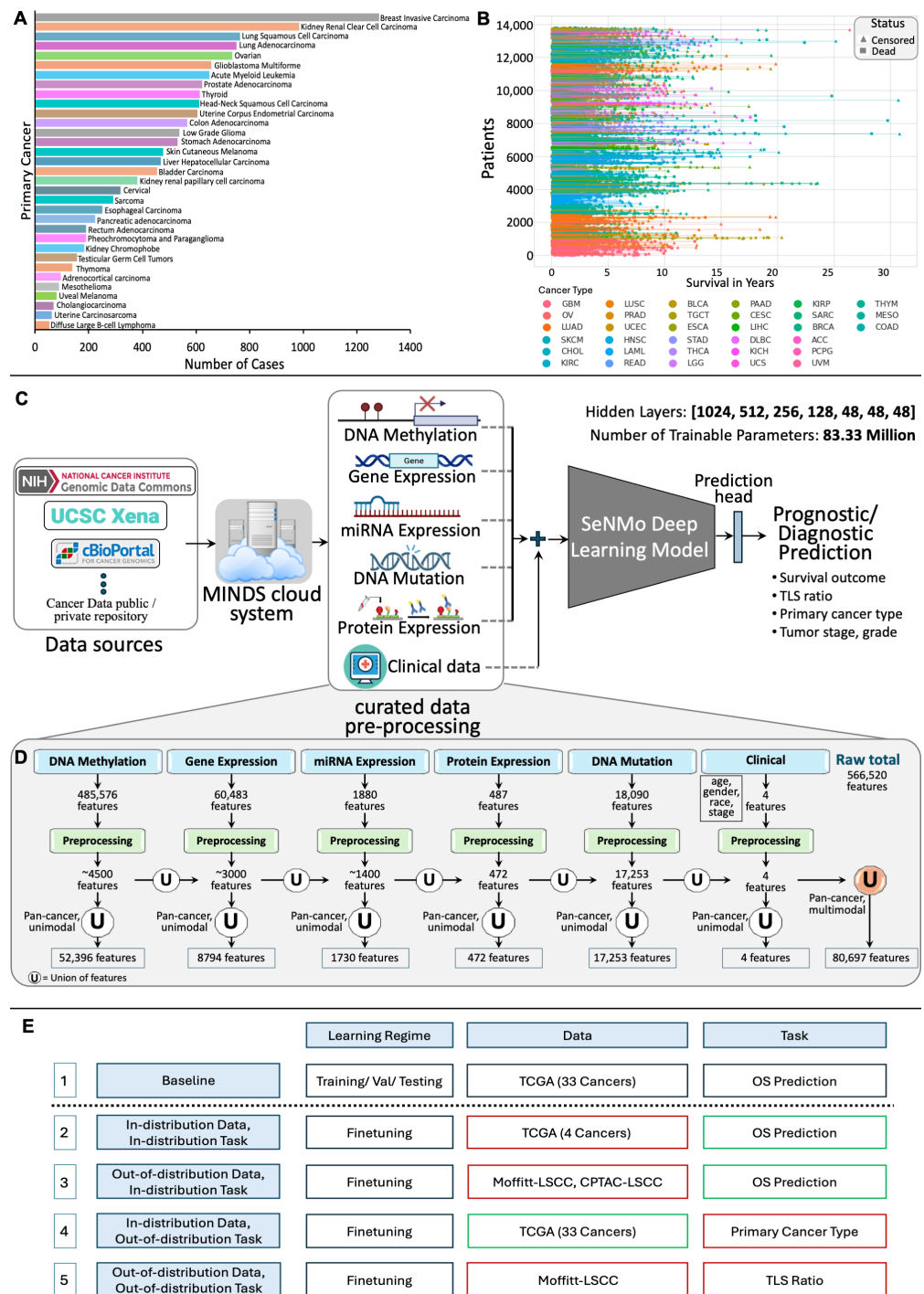


**Figure 1.** (A): Number of cases for each cancer type, highlighting variation in sample sizes across cancers. (B): Patient survival in years, with each line representing an individual patient, marked as censored or dead, and grouped by cancer type. (C): Overview of the SeNMom framework. The data from public and private sources are collected using Multimodal Integration of Oncology Data System (MINDS) [3] and curated to develop the multiomics dataset. The learned model weights are later used for different downstream prognostic and diagnostic tasks. (D): Features processing pipeline for six data types. Initial modality features reduced through preprocessing are unified at pan-cancer level to yield unimodal pan-cancer feature sets, which are further unified across modalities, resulting in a multiomics matrix of 80,697 features. (E): Study design and simulations for SeNMom across different learning regimes, datasets, and tasks. The baseline model (row 1) is first trained on TCGA data with 33 cancer types for overall survival prediction. Rows 2–5 represent in-distribution data/ task (same as baseline) and out-of-distribution data/ task (different from baseline) variations: red-bordered boxes indicate a change from the baseline, while green-bordered boxes align with the baseline.

This study presents the first unified framework for pan-cancer multi-omics modeling that jointly supports prognostic and diagnostic tasks using a self-normalizing neural architecture. SeNMo demonstrates strong performance in predicting OS, accurately classifying 33 primary cancer types, and estimating TLS ratios from molecular data alone. By incorporating six distinct data modalities and enabling transfer to external cohorts through fine-tuning, SeNMo addresses key limitations of existing models in scalability, robustness, and clinical relevance. Beyond model performance, we contribute the learned patient features (also called embeddings) generated from our model to an open-access latent embedding resource [4], which facilitates further exploration and reuse of the SeNMo's learned representations. Taken together, our work advances the development of integrative, modality-robust models for multi-omics oncology applications and sets the stage for broader translational use of deep learning in cancer prognosis and diagnosis.

## 2. Results

### 2.1. Prognostic Modeling: Overall Survival (OS)

**Pan-cancer performance:** Figure 2 summarizes SeNMo's prognostic ability when trained on the full six-modal TCGA dataset and evaluated on the held-out test set. The inference on the test set showed the C-Index of 0.757, the average of the C-Indices from the 10 checkpoints. To further validate our findings, we created an ensemble of the 10 checkpoints by averaging the prediction vectors from all the models and then evaluating the final averaged prediction vector for C-Index. For the pan-cancer, multi-omics data, SeNMo achieved an ensemble C-Index of 0.758 on the held-out test set. The significance level in all these analyses is 95%, i.e.,  $p < 0.05$ , indicating statistically significant values. Training and validation trajectories are provided in Figure A4.

**Impact of missing modalities:** Modality ablation experiments confirmed that performance degraded gracefully as data layers were withheld. Using only gene-expression inputs, SeNMo achieved test/ensemble C-indices of 0.718/0.728, respectively. DNA-methylation alone yielded 0.644/0.650, and miRNA alone 0.686/0.702. Combining the three transcriptomic layers recovered much of the full-model performance (0.725/0.726). Adding protein (4-modal) data increased the C-index to 0.746/0.751, while adding mutation (5-modal) data resulted in the C-indices of 0.746/0.749.

**Tumor-specific generalization:** Applied cancer by cancer on the held-out test set for each of 33 tumor types, the six-modal model achieved statistically significant ( $p < 0.05$ ) C-indices in 29 cancers (Figure 3; Table 1). The best performance occurred in pheochromocytoma and paraganglioma (TCGA-PCPG) with test/ensemble C-indices of 0.900/0.929. Four cohorts (GBM, LAML, PRAD, TGCT) initially fell below significance. Targeted fine-tuning for ten epochs raised the C-indices for GBM, LAML, and PRAD to 0.642/0.650, 0.627/0.626, and 0.541/0.542, respectively, while TGCT was still not statistically significant (i.e.,  $p > 0.05$ ) and proved to be a failure case for this study.

**External validation:** External evaluation demonstrated robustness to domain shift. Zero-shot transfer to CPTAC-LSCC and an independent Moffitt-LSCC cohort produced test/ensemble C-indices of 0.48/0.50 and 0.581/0.590, respectively. A brief ten-epoch fine-tune elevated these scores to 0.677/0.730 (CPTAC-LSCC) and 0.647/0.656 (Moffitt-LSCC), illustrating efficient domain adaptation. These results are highlighted in green box-plots of Figure 3.

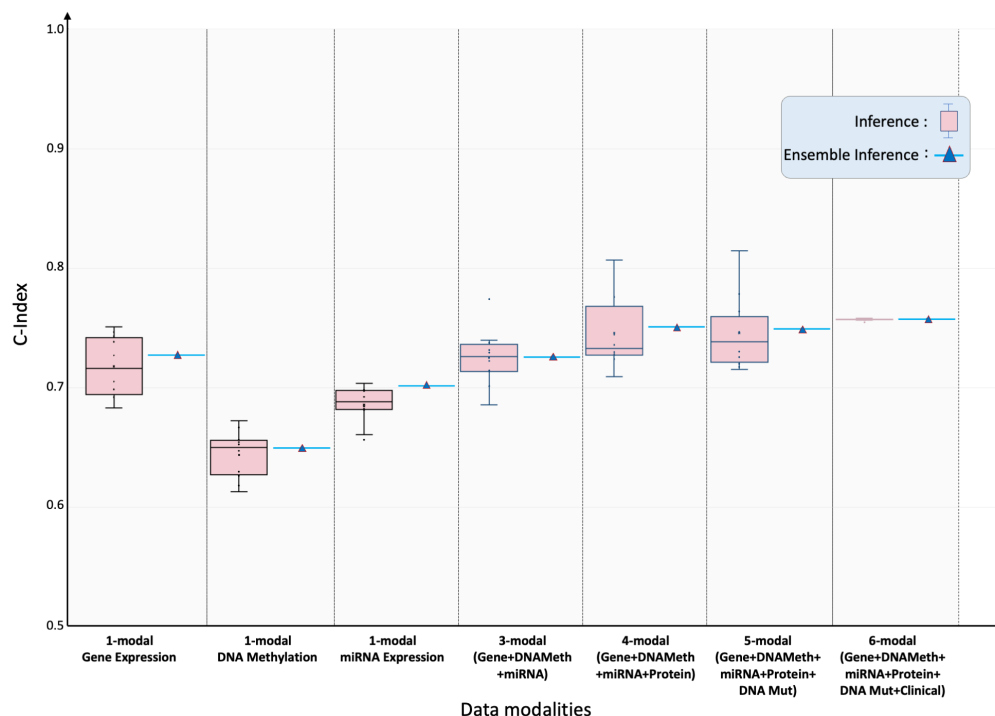


**Figure 2.** Pan-cancer concordance indices for overall-survival prediction under incremental modality integration. SeNMmo model was trained and evaluated, using different combinations of data modalities, on 80% of the total data, and evaluated on the 20% held-out test set. Box-plots summarize ten-fold cross-validation results for models ingesting 1-, 3-, 4-, 5- and 6-modal input configurations. As the number of modalities increased, the model’s performance improved, confirming additive prognostic value from each modality. All scores surpass the 95% significance threshold (log-rank  $p < 0.05$ ).

**Table 1.** C-Index for test and ensemble inference across cancer types.

Cancer Type	C-Index {Test, Ensemble}	Cancer Type	C-Index {Test, Ensemble}
TCGA-PCPG	{0.900, 0.929}	TCGA-DLBC	{0.714, 0.619}
TCGA-ACC	{0.866, 0.861}	TCGA-MESO	{0.599, 0.615}
TCGA-UVM	{0.822, 0.829}	TCGA-LUSC	{0.588, 0.592}
TCGA-LGG	{0.821, 0.823}	TCGA-PAAD	{0.597, 0.598}
TCGA-KICH	{0.801, 0.807}	TCGA-HNSC	{0.583, 0.583}
TCGA-KIRC	{0.777, 0.776}	TCGA-CHOL	{0.574, 0.574}
TCGA-KIRP	{0.775, 0.778}	TCGA-COAD	{0.546, 0.542}
TCGA-UCEC	{0.708, 0.713}	TCGA-THYM	{0.555, 0.571}
TCGA-THCA	{0.696, 0.698}	TCGA-UCS	{0.514, 0.541}
TCGA-SKCM	{0.691, 0.689}	TCGA-OV	{0.518, 0.509}
TCGA-BRCA	{0.687, 0.692}	TCGA-READ	{0.550, 0.551}
TCGA-CESC	{0.676, 0.682}	TCGA-GBM	{0.642, 0.650} *
TCGA-ESCA	{0.650, 0.648}	TCGA-LAML	{0.627, 0.626} *
TCGA-LUAD	{0.647, 0.653}	TCGA-PRAD	{0.541, 0.542} *
TCGA-SARC	{0.650, 0.658}	TCGA-STAD	{0.631, 0.628}
TCGA-LIHC	{0.627, 0.629}	TCGA-BLCA	{0.609, 0.609}
		TCGA-TGCT	{0.123, 0.091} **

\* after few-shots fine-tuning because inference on baseline was not statistically significant ( $p > 0.05$ ); \*\* failure case.

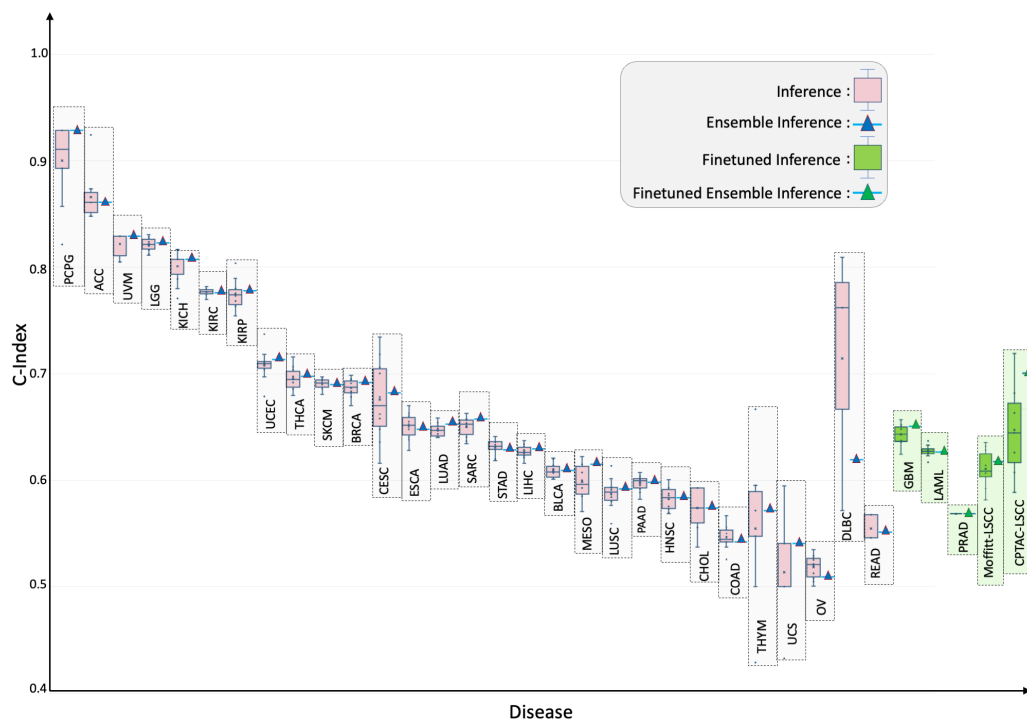


**Figure 3.** Tumor-specific concordance indices for SeNMö across 32 cancer types and two external lung-squamous cohorts. Pink box-plots depict zero-shot predictions on each held-out TCGA subset; green box-plots show outcomes after a brief ten-epoch fine-tune where baseline performance was not significant or the cohort was unseen (CPTAC-LSCC, Moffitt-LSCC). Ensemble estimates are indicated by triangles. Although trained on pan-cancer cohort, SeNMö effectively captures survival times across individual cancers. Fine-tuning improved performance for cases with initially low predictive significance, and markedly improved external-cohort accuracy, illustrating SeNMö’s capacity for rapid domain adaptation.

**Risk stratification:** We further investigated the SeNMö’s ability to stratify the patients based on low, intermediate, and high risk conditions. We generate Kaplan–Meier (KM) curves of our model on the pan-cancer, multi-omics held-out test set, as shown in Figure 4. We selected the low/intermediate/high risk terciles stratification as the 33–66–100 percentile of hazard predictions [5,6]. The hazard scores predicted by SeNMö are used to evaluate the model’s stratification ability. The KM comparative analysis shows that SeNMö distinguished the patients across the three groups. The low-risk group (green) exhibited the highest survival probability, maintaining close to 100% survival up to approximately 5 years, and gradually declining to about 60% by the 25-year mark. The intermediate-risk group (blue) showed a significantly lower survival probability, starting to diverge from the low-risk group early on and reaching around 40% by the 15-year mark of the study period. The high-risk group (orange) displayed the most pronounced decline in survival probability, with a steep drop to approximately 20% survival within the first 10 years, and further reducing to below 10% after 10 years. The logrank test to evaluate the significance of this stratification shows that the  $p$ -value of low vs. intermediate curves is  $1.66 \times 10^{-5}$ , low vs. high is  $1.16 \times 10^{-46}$ , and intermediate vs. high is  $1.92 \times 10^{-22}$ , showing significant results, i.e.,  $p < 0.05$ . The 95% confidence intervals around each curve show the stability of these estimates.

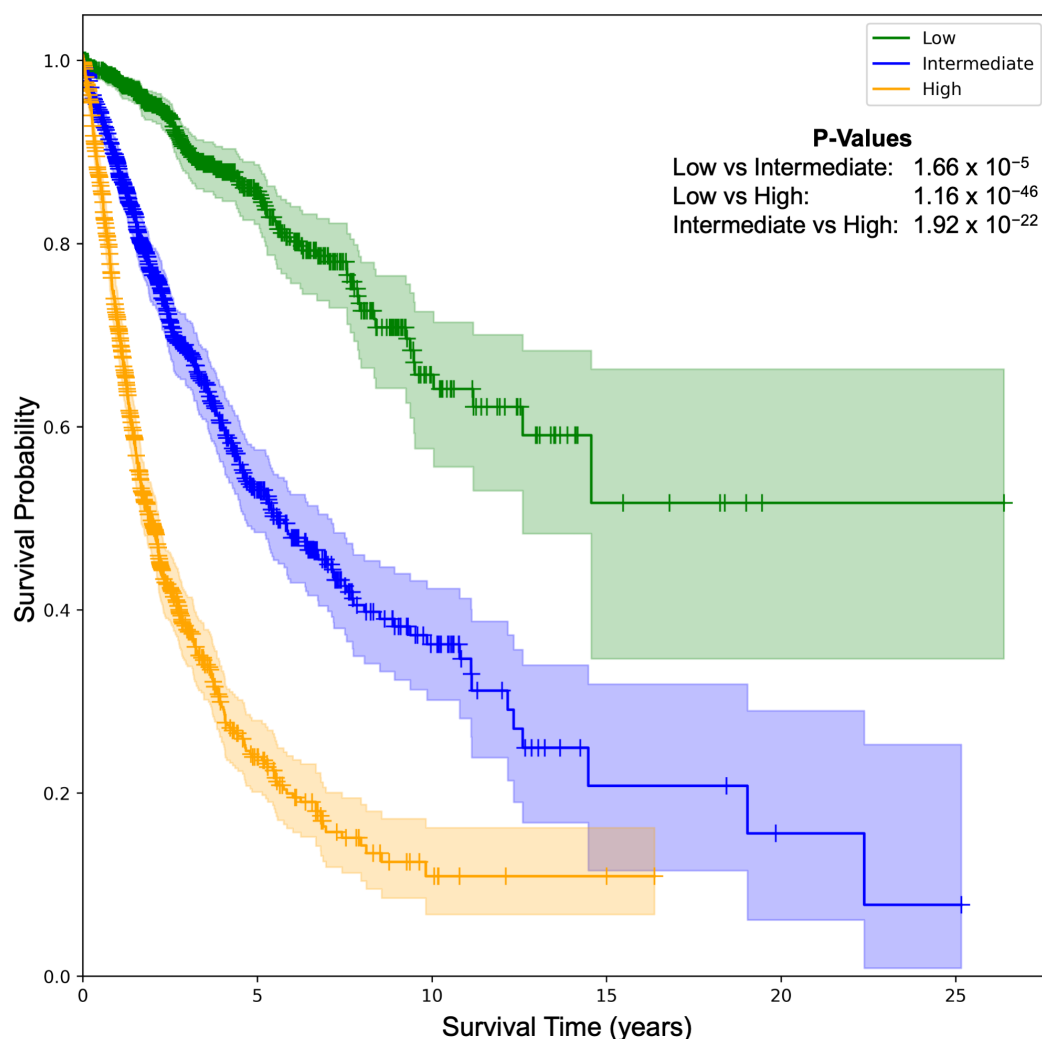


**Figure 4.** Kaplan–Meier (KM) survival curves illustrating SeNMo-driven risk stratification on the pan-cancer data. Patients are partitioned into low, intermediate, and high-risk terciles using the 33rd and 66th percentiles of predicted hazard scores. Survival trajectories diverge markedly across strata. The  $p$ -values from logrank test for Low vs. Intermediate:  $1.66 \times 10^{-5}$ , Low vs. High:  $1.16 \times 10^{-46}$ , and Intermediate vs. High:  $1.92 \times 10^{-22}$ . The shaded areas around each curve depict the 95% confidence intervals.

## 2.2. Diagnostic Modeling: Primary Cancer Type Classification

**Primary cancer type classification:** To test the generalizability of SeNMo to diagnostic tasks, we carried out the prediction of primary cancer type from pan-cancer, multi-omics data. Excluding the *stage* variable from the clinical covariates to avoid label leakage, we framed cancer identification as a 33-way classification task. When considering a cancer type classification problem, the stage adds a bias in the data because of the staging distribution among different cancers. SeNMo achieved near-perfect discrimination with mean training accuracy of 99.9%, validation accuracy of 99.8%, and identical 99.8% accuracy for both single-checkpoint and ensemble inference (Table 2, Figure A5).

**Error distribution:** The confusion matrix (Figure A5) depicts a clear concentration of values along the diagonal, indicating a high rate of correct predictions across all cancer types. Residual misclassifications are restricted to biologically related pairs (e.g., colon vs. rectal adenocarcinoma). The scatter plot shows an alignment of predicted labels with true labels along the diagonal line, highlighting the model’s robust predictive accuracy.

**Per-class metrics:** The classification report across various cancer types reveals that the model consistently maintains high precision, recall, and F1-scores for all tumor types,

reflecting balanced sensitivity and specificity across the highly imbalanced class distribution. Detailed values are provided in Table 2.

Interpretation: The model’s diagnostic power highlights the distinct molecular signatures captured across gene expression, DNA methylation, miRNA abundance, protein levels and mutational spectra. These results demonstrate that SeNMo’s unified representation retains class-specific signals despite training jointly on heterogeneous modalities and objectives.

**Table 2.** Classification report of different diseases with precision, recall, F1-score, and support metrics across 33 cancer types.

Primary Site	Data	Class	Precision	Recall	F1-Score	Support
Adrenocortical	TCGA-ACC	0	1	1	1	16
Bladder	TCGA-BLCA	1	1	1	1	89
Breast	TCGA-BRCA	2	1	1	1	245
Cervical	TCGA-CESC	3	1	1	1	62
Bile Duct	TCGA-CHOL	4	1	1	1	8
Colon	TCGA-COAD	5	0.99	1	1	108
Large B-cell Lymphoma	TCGA-DLBC	6	1	1	1	10
Esophageal	TCGA-ESCA	7	1	1	1	44
Glioblastoma	TCGA-GBM	8	0.94	1	0.97	48
Head and Neck	TCGA-HNSC	9	1	1	1	121
Kidney Chromophobe	TCGA-KICH	10	1	1	1	12
Kidney Clear Cell Carcinoma	TCGA-KIRC	11	1	1	1	146
Kidney Papillary Cell Carcinoma	TCGA-KIRP	12	1	1	1	71
Acute Myeloid Leukemia	TCGA-LAML	13	1	1	1	22
Lower Grade Glioma	TCGA-LGG	14	1	1	1	107
Liver	TCGA-LIHC	15	1	1	1	87
Lung Adenocarcinoma	TCGA-LUAD	16	1	1	1	126
Lung Squamous Cell Carcinoma	TCGA-LUSC	17	0.98	0.99	0.99	113
Mesothelioma	TCGA-MESO	18	1	1	1	18
Ovarian	TCGA-OV	19	1	1	1	104
Pancreatic	TCGA-PAAD	20	1	1	1	121
Pheochromocytoma & Paraganglioma	TCGA-PCPG	21	1	1	1	38
Prostate	TCGA-PRAD	22	1	1	1	117
Rectal	TCGA-READ	23	1	1	1	23
Sarcoma	TCGA-SARC	24	1	1	1	52
Skin Cutaneous Melanoma	TCGA-SKCM	25	1	1	1	96
Stomach	TCGA-STAD	26	1	1	1	121
Testicular	TCGA-TGCT	27	1	1	1	25
Thyroid	TCGA-THCA	28	1	1	1	97
Thymoma	TCGA-THYM	29	1	1	1	24
Endometrioid	TCGA-UCEC	30	1	1	1	193
Uterine Carcinosarcoma	TCGA-UCS	31	1	1	1	11
Uveal melanomas	TCGA-UVM	32	1	1	1	16
Weighted Avg			<b>1</b>	<b>1</b>	<b>1</b>	<b>2360</b>

### 2.3. Immune Microenvironment Modeling: TLS Ratio Prediction

TLS ratio estimation as a window into the immune micro-environment: To test whether SeNMo's latent representation captures micro-environmental cues, we fine-tuned the backbone on a cohort of lung-squamous cell carcinoma data from Moffitt Cancer Center to predict the tissue-level TLS ratio (segmented TLS area/total tissue area). The task was formulated as a single-output regression problem. The SeNMo baseline model was subjected to few-shots fine-tuning using the cross-validation on 76 patients (80%) and evaluated on the held-out 20-patient (20%) cohort, as shown in Figure 5.

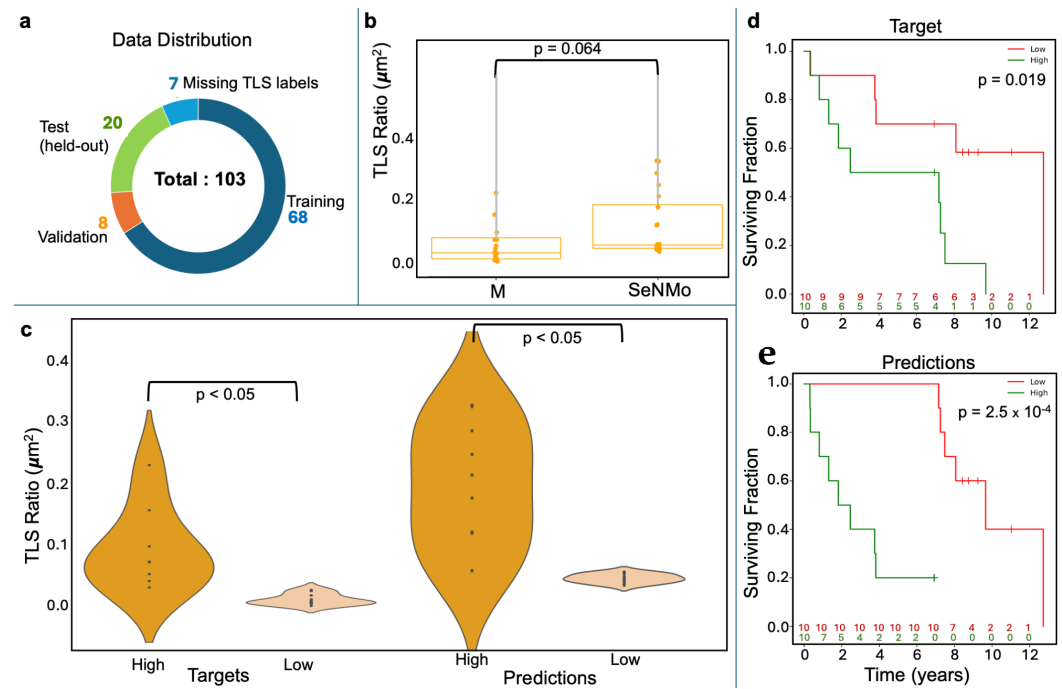


**Figure 5.** Tertiary Lymph Structures (TLSs) ratio predictions by SeNMo. (a) Dataset distribution, dividing 103 samples into training, validation, test, and excluding those missing TLS data. (b) Box plots compare TLS ratios between manual annotations (M) and SeNMo predictions, showing no significant difference ( $p = 0.064$ ). (c) Violin plot of TLS Ratio annotations for high vs. low groups thresholded by the median value, with a significant difference ( $p < 0.05$ ). (d) Violin plot of SeNMo's TLS Ratio predictions, also showing significant separation between high and low groups ( $p < 0.05$ ). (e) Kaplan–Meier survival curves with significant survival differences, comparing high vs. low TLS ratios for both annotations (top,  $p = 0.019$ ) and SeNMo predictions (bottom,  $p = 2.5 \times 10^{-4}$ ).

**Concordance with expert assessment:** On the held-out test set, SeNMo's continuous TLS predictions were significantly similar to manual annotations (Figure 5b); a paired comparison found no significant mean difference ( $p = 0.064$ ), confirming close agreement.

**Discriminating high versus low TLS burden:** Violin plots illustrate the separation between manually defined high/low TLS groups and the corresponding SeNMo-predicted groups (Figure 5c). In both cases the distributions differ significantly ( $p < 0.05$ ), indicating that the model preserves biologically meaningful thresholds.

**Prognostic relevance of modeled TLS ratios:** Kaplan–Meier analysis demonstrates that patients stratified by either manual or SeNMo-predicted TLS ratio exhibit distinct survival outcomes. Manual labels yield a log-rank  $p = 0.019$ , while SeNMo-based stratification improves the signal to  $p = 2.5 \times 10^{-4}$  (Figure 5d). These findings show that the learned representations not only reproduce pathologist assessments but also retain prognostic power.

### 3. Discussion

SeNMo integrates five omics layers and clinical covariates within a self-normalizing architecture to deliver a unified representation that performs strongly across prognostic, diagnostic, and immune-profiling tasks. We analyzed a pan-cancer dataset of multiple cancer types (with varying amounts of features) using our SeNMo encoder-based framework. Public databases such as CPTAC and TCGA contain common identifiers within their data that connect data from the same patient. Therefore, molecular data, such as gene expression, miRNA expression, DNA methylation, somatic mutations, and protein expression can be consolidated to represent a singular patient. However, such high-dimensional data has intra- and inter-dataset correlations, heterogeneous measurement scales, missing values, technical variations, and other forms of noise [7]. The concordance indices achieved for overall survival (up to 0.758 pan-cancer and 0.730 after domain adaptation) have been shown to outperform the existing works in OS prediction when considering the data modalities included in our data [8]. Moreover, we observed that adding more data and types of modalities increased the model's performance. Crucially, SeNMo maintains performance when modalities are missing, confirming the utility of self-normalizing layers for handling heterogeneous, sparsely observed inputs. After extensive training-evaluation runs, we found, through optimal parameter searching, a model that performs very well across the different data types and tasks (refer to Figures A3 and A4).

The model's performance was evaluated on individual cancers at test-time through simple inference and ensembling methods. We observed that the model's predictive power improved when an ensemble of the checkpoints was employed (refer to Figure 3). However, for the four cancer types, TCGA-GBM, TCGA-LAML, TCGA-PRAD, and TCGA-TGCT, the model did not show significant predictive power. During the investigation, we observed that these datasets had non-admissible pairs in some of the data folds, i.e., all samples had censor value  $\delta = 0$  (refer to Equation (A5)). In the case of TCGA-PRAD and TCGA-TGCT, the number of samples having  $\delta = 1$  in the training/validation cohort was 12 and 3, respectively. To address the lack of predictive power, we fine-tuned the model for these datasets by using the stratified k-folds to offset the class-representation problem in the data folds. After searching for the optimal hyperparameters for fine-tuning, the model's performance became significant ( $p < 0.05$ ) for three out of four datasets (refer to green box plots in Figure 3). Moreover, the TCGA-CDR consortium has already cautioned that OS is not recommended for TGCT owing to an insufficient number of events [9]. Figure 4 shows that tercile-based hazard scores sharply separate survival curves, spotlighting patients who need intensified care while identifying those with favorable prognoses. This clear gradient supports personalized treatment planning and evidence-guided follow-up to improve overall survival across diverse cohorts.

From a diagnostic perspective, cancer type classification is routinely studied for early detection and localization of tissue of origin [10]. The classification results in Table 2 illustrate the superior generalizability of the model's predictive power to classify primary cancer types through the SeNMo encoder, despite it being primarily trained for predicting OS. Additionally, the detailed classification report across various cancer types reveals that the model consistently maintains high precision, recall, and F1-scores for almost all cancer types. Such metrics not only confirm the model's effectiveness in accurately identifying the correct cancer class but also its reliability in replicating these results across different samples. This level of performance suggests the capability of the model to successfully learn high level representations from heterogeneous, high-dimension, multivariate data stemming from complex molecular modalities such as gene expression, miRNA expression, somatic mutations, DNA methylation, and protein expression. Previous multi-omics classifiers often

require modality-specific encoders or extensive feature engineering [11]; SeNMo achieves superior accuracy with a single backbone, simplifying deployment and maintenance.

Fine-tuning for TLS ratio prediction demonstrates that SeNMo's latent space captures micro-environmental information not explicitly provided during pre-training. As shown in Figure 5, SeNMo's ability to predict TLS ratios was evaluated on an unseen cohort of lung squamous cell carcinoma data from Moffitt Cancer Center. The comparison between manual TLS ratio annotations and SeNMo-predicted values showed no significant difference, indicating a high level of concordance between human annotations and model predictions. Violin plots depicting high vs. low TLS ratio groups—both for manual and SeNMo predictions—revealed significant separation, demonstrating the model's robustness in distinguishing between biologically distinct TLS levels. Furthermore, KM survival curves for high vs. low TLS ratio groups revealed significant differences in survival outcomes, with stronger statistical significance observed for SeNMo-predicted data compared to manual annotations. The ability to reproduce pathologist TLS assessments and enhance survival stratification after minimal adaptation suggests that the model learns transferable features spanning tumor-intrinsic and immune contexts. This dual capacity is valuable for applications such as immunotherapy response prediction, where both tumor genetics and immune infiltration matter [12]. Overall, the results indicate that SeNMo can successfully generalize to new tasks and datasets, accurately predicting TLS ratios and offering valuable prognostic insights that could improve clinical decision-making.

It is imperative to mention here that MLP-based networks are very sensitive to catastrophic forgetting when presented with out-of-distribution data or when subjected to a different task [13]. We fine-tuned the SeNMo encoder for one public dataset (CPTAC-LSCC) and one internal dataset (Moffitt's LSCC) [14,15]. In our simulations to fine-tune the model, we encountered the catastrophic forgetting phenomenon in SeNMo, where the model would fail to converge on both new datasets. This was more pronounced when a certain number of hidden layers were frozen, and the rest were trained with lower learning rates. We resorted to the option of unfreezing all the layers of the encoder and fine-tuning the model with a very small learning rate ( $4 \times 10^{-5}$ ), high weight decay and dropout (0.35), and just 10 epochs. This method worked, and the model showed significant performance on the out-of-distribution datasets.

SeNMo's unified architecture enables simultaneous estimation of survival risk, tumor origin, and immune context from the same patient profile, streamlining molecular decision-support workflows. In settings with incomplete data, which is common in routine oncology practice, the model degrades gracefully, allowing actionable output even when only transcriptomics are available. The strong external performance on CPTAC-LSCC and Moffitt-LSCC shows that the learned representation transfers across sequencing platforms and institutional pipelines after brief calibration. Because of the modular structure of SeNMo, its data-ingestion layer can accept any external normalization, e.g., RNA-seq matrices processed with limma-voom [16] or the DESeq2 variance-stabilizing transform [17] can be routed into the same encoder, while the other omics tracks retain the default log+z pipeline. This plug-and-play design lets researchers incorporate task-specific preprocessing or differential-expression outputs without modifying the network architecture, enabling seamless extension of the framework to future modality-specific workflows.

There are some limitations to this work that warrant discussion. First, despite robust overall performance, four cancer types exhibited low baseline C-indices and one (TGCT) remained refractory to fine-tuning, indicating that tumor-specific molecular peculiarities can still elude the shared model. Second, the external validation cohorts were confined to one internal and one public data cohort; broader evaluation across additional histologies will further substantiate generalizability. Third, TLS labels were derived from image-analysis

pipelines, incorporating an image-based deep learning encoder would potentially automate this process and reduce the measurement noise. The research community is invited to advance this work in future; some avenues of exploration include (i) contrastive pre-training with synthetic modality dropout to enhance robustness, (ii) incorporation of spatial transcriptomics and digital pathology features to better characterize micro-environmental heterogeneity, (iii) inclusion of other molecular data modalities such as mRNA, CNVs/CNAs by adapting the SeNMo’s encoder to variable input size and adding a fine-tuning head for downstream prediction, and (iv) prospective validation within molecular tumor boards to quantify clinical impact on treatment decisions.

### 4. Materials and Methods

Figure 1 presents the outline of this work that includes the data types and characteristics (Figure 1A,B), preprocessing and model development (Figure 1C,D), and the study design and simulations (Figure 1E). Below, we discuss each of these steps in detail.

#### 4.1. Data Acquisition

TCGA houses one of the largest collections of high-dimensional multi-omics datasets, comprising over 20,500 individual tumor samples from 33 different cancer types [18]. The available data includes high-throughput RNA sequencing (RNA-Seq), DNA sequencing (DNA-Seq), microRNA sequencing (miRNA-Seq), single nucleotide variants, copy number variations, DNA methylation, and reverse-phase protein array (RPPA) data [18]. Building cohorts from this diverse data, spanning multiple formats, modalities, and systems, presents significant challenges. To curate and establish patient cohorts, we utilized our previously developed Multimodal Integration of Oncology Data System (MINDS), a meta-data framework designed to fuse data from publicly available sources like TCGA-GDC and UCSC Xena Portal into a machine learning-ready format [3,18,19]. MINDS is freely accessible to the cancer research community and has been integrated into the SeNMo framework to enhance its usability and benefit to researchers. For training, validation, and testing, we used pan-cancer data from TCGA and Xena, covering 33 cancer types. We further fine-tuned the model using data from the CPTAC-LSCC [14] and Moffitt’s LSCC datasets [15] to evaluate the generalizability and transfer learning capabilities of SeNMo. The details of clinical data characteristics are given in Table 3.

**Table 3.** Summary of patient characteristics for pan-cancer data in this study.

Cancer Type	Age (Mean ± SD)	Gender (M/F)	Race (White/Asian/Black/NA/American Indian/Alaska)	Stage (0/I/IIA/IB/IC/II/IIA/IIIB/IIIC/III/IIIA/IIIB/IIIC/IV/IVA/IVB/IVC/NA)
TCGA-ACC	47.46 ± 16.20	33/62	79/3/1/12/0	0/9/0/0/0/46/0/0/0/20/0/0/0/17/0/0/0/3
TCGA-BLCA	67.92 ± 10.39	326/121	363/43/23/18/0	0/3/0/0/0/136/0/0/0/159/0/0/0/148/0/0/0/1
TCGA-BRCA	57.94 ± 13.11	13/1247	915/59/198/87/1	0/114/94/7/0/6/404/307/0/2/176/30/74/22/0/0/0/24
TCGA-CESC	48.04 ± 13.70	0/304	211/19/32/30/9	0/0/0/0/0/0/0/0/0/0/0/0/0/0/0/0/0/304
TCGA-CHOL	64.37 ± 12.21	30/32	55/3/3/1/0	0/30/0/0/0/16/0/0/0/5/0/0/0/2/3/6/0/0
TCGA-COAD	66.93 ± 12.67	288/251	261/11/67/198/2	0/87/1/0/0/46/150/13/2/26/9/69/47/56/18/3/0/12
TCGA-DLBC	56.76 ± 13.68	24/27	32/18/1/0/0	0/0/0/0/0/0/0/0/0/0/0/0/0/0/0/0/51
TCGA-ESCA	64.22 ± 12.11	208/41	162/46/6/35/0	0/14/9/7/0/1/56/43/0/41/16/10/9/7/6/0/0/30
TCGA-GBM	57.74 ± 14.32	399/250	547/13/53/36/0	0/0/0/0/0/0/0/0/0/0/0/0/0/0/0/0/649
TCGA-HNSC	61.02 ± 11.92	443/168	522/12/58/17/2	0/29/0/0/0/93/0/0/0/97/0/0/0/0/302/13/1/76
TCGA-KICH	51.61 ± 14.12	99/83	154/6/19/3/0	0/75/0/0/0/59/0/0/0/34/0/0/0/14/0/0/0/0
TCGA-KIRC	60.67 ± 11.95	641/338	876/16/73/14/0	0/475/0/0/0/102/0/0/0/237/0/0/0/161/0/0/0/4
TCGA-KIRP	61.98 ± 12.20	278/98	275/6/75/16/4	0/219/0/0/0/25/0/0/0/77/0/0/0/21/0/0/0/34
TCGA-LAML	54.82 ± 15.87	345/281	564/8/49/5/0	0/0/0/0/0/0/0/0/0/0/0/0/0/0/0/0/626
TCGA-LGG	42.71 ± 13.32	293/240	492/8/22/10/1	0/0/0/0/0/0/0/0/0/0/0/0/0/0/0/0/533
TCGA-LIHC	60.44 ± 13.71	305/158	255/168/25/14/1	0/211/0/0/0/105/0/0/0/6/78/12/11/2/1/3/0/34
TCGA-LUAD	65.20 ± 10.08	329/399	580/14/84/48/2	0/7/194/195/0/2/67/103/0/0/101/12/0/37/0/0/0/10
TCGA-LUSC	67.28 ± 8.62	548/204	530/12/47/163/0	0/4/127/243/0/4/87/138/0/3/94/33/0/12/0/0/0/7
TCGA-MESO	63.01 ± 9.78	70/16	84/1/1/0/0	0/7/2/1/0/15/0/0/0/45/0/0/0/16/0/0/0/0
TCGA-OV	59.60 ± 11.44	0/731	626/25/43/33/3	0/0/0/0/0/0/0/0/0/0/0/0/0/0/0/0/731
TCGA-PAAD	64.87 ± 11.36	123/99	195/13/8/6/0	0/1/6/15/0/0/36/148/0/6/0/0/0/7/0/0/0/3



- Drop constant features: Next, constant/quasi-constant features with a threshold of 0.998 were filtered out using Feature-engine, a Python library for feature engineering and selection [24]. The threshold was selected so as to remove only the features with no expression at all across every sample and also features that had high noise contents, since the expression value was the same across every sample.
- Remove duplicates features: Next, duplicate features between genes were identified that contained the same values across two separate genes, and one of the genes was kept. This may reveal gene–gene relationships between the two genes stemming from an up-regulation pathway or could simply reflect noise.
- Remove colinear features: Next, we filtered the features having low variance ( $\approx 0.25$ ) because the features having high variance hold the maximum amount of information [25]. We used the VarianceThreshold feature selector of scikit learn library that removes low-variance features based on the defined threshold [26]. We chose a threshold for each data modality so that the resulting features have matching dimensions, as shown in Figure 1D.
- Remove low-expression genes: The gene expression data originally contained 60,483 features, with FPKM transformed numbers ranging from 0 to 12. Roughly 30,000 features remained after the above-mentioned preprocessing steps, which was still a very high number of features. High expression values reveal important biological insights due to an indication that a certain gene product is transcribed in large quantities, revealing their relevance compared to low expression values [27]. Although there is no well-defined consensus on the selection of cut-off value, existing practices involve keeping high-variance and high-expression values [28–31]. Based on evidence from existing literature and our empirical analysis on the resultant feature dimension [30,31], features containing an expression value greater than 7 (127 FPKM value) were kept for our simulations.
- Handle missing features: We handled missing features at two levels of data integration. First, for the features within each modality and cancer type, the missing values were imputed with the mean of the samples for that feature. This resulted in the full-length feature vector for each sample. Second, across different cancers and modalities, we padded the missing features with zeros. In deep learning, the zero imputation technique shows the best performance compared to other imputation techniques and deficient data removal techniques [32–34].

#### 4.4. Features Integration

After preprocessing, the data is integrated across cancers and modalities, generating two views: one by unifying features across all patients within each modality, and second by combining all modalities. Feature dimension post-preprocessing includes DNA methylation (reduced from 485,576 to  $\sim 4500$  per patient, unionized to 52,396), gene expression (60,483 to  $\sim 3000$  per patient, unionized to 8794), miRNA expression (1880 to  $\sim 1400$  per patient, unionized to 1730), protein expression (487 to 472), and DNA mutation (18,090 to 17,253). Details of these feature reductions and integrations are summarized in Table 4. In addition to integrating these multi-omics data, we also integrate four clinical data features, including age, gender, race, and cancer stage. These features are added to the combined multi-omics feature through concatenation, resulting in the per-sample feature dimension of 80,697. Mathematically, the integration is explained below.

$$V_m = \begin{cases} \bigcup_{i=1}^n \tilde{v}_i & \text{if } \tilde{v}_i \text{ varies by cancer type or modality,} \\ \tilde{v} & \text{otherwise.} \end{cases} \quad (1)$$

Finally, the union of all  $V_m$  across different modalities results in the total pan-cancer, multimodal feature vector  $V_c \in \mathbb{R}^{80,697}$ , expressed as:

$$V_c = \bigcup_{m=1}^M V_m \quad (2)$$

**Table 4.** Feature reduction summary of pan-cancer data.

Data (TCGA-GDC)	Primary Site	Cases	miRNA Exprn		DNA Methyl		Gene Exprn		Protein Exprn		DNA Mut	
			Before	After	Before	After	Before	After	Before	After	Before	After
TCGA-DLBC	Large B-cell Lymphoma	51	1880	1060	485,576	4396	60,483	850	487	472	18,090	17,253
TCGA-UCS	Uterine Carcinosarcoma	61	1880	1101	485,576	4632	60,483	1231	487	472	18,090	17,253
TCGA-CHOL	Bile Duct	62	1880	967	485,576	4479	60,483	1261	487	472	18,090	17,253
TCGA-UVM	Uveal melanomas	80	1880	1162	485,576	4019	60,483	772	487	472	18,090	17,253
TCGA-MESO	Mesothelioma	86	1880	1158	485,576	4372	60,483	1278	487	472	18,090	17,253
TCGA-ACC	Adrenocortical	95	1880	1110	485,576	4454	60,483	1304	487	472	18,090	17,253
TCGA-THYM	Thymoma	138	1880	1245	485,576	4609	60,483	1337	487	472	18,090	17,253
TCGA-TGCT	Testicular	139	1880	1290	485,576	4762	60,483	1343	487	472	18,090	17,253
TCGA-READ	Rectal	178	1880	1314	485,576	4077	60,483	1547	487	472	18,090	17,253
TCGA-KICH	Kidney Chromophobe	182	1880	1089	485,576	4333	60,483	1107	487	472	18,090	17,253
TCGA-PCPG	Pheochromocytoma and Paraganglioma	189	1880	1251	485,576	4550	60,483	1216	487	472	18,090	17,253
TCGA-PAAD	Pancreatic	222	1880	1308	485,576	4518	60,483	1567	487	472	18,090	17,253
TCGA-ESCA	Esophageal	249	1880	1300	485,576	4192	60,483	1684	487	472	18,090	17,253
TCGA-SARC	Sarcoma	287	1880	1235	485,576	4467	60,483	2490	487	472	18,090	17,253
TCGA-CESC	Cervical	304	1880	1405	485,576	4167	60,483	2017	487	472	18,090	17,253
TCGA-KIRP	Kidney Papillary Cell Carcinoma	376	1880	1297	485,576	4078	60,483	1798	487	472	18,090	17,253
TCGA-SKCM	Skin Cutaneous Melanoma	436	1880	1426	485,576	4427	60,483	2488	487	472	18,090	17,253
TCGA-BLCA	Bladder	447	1880	1361	485,576	4483	60,483	2751	487	472	18,090	17,253
TCGA-LIHC	Liver	463	1880	1336	485,576	4023	60,483	2017	487	472	18,090	17,253
TCGA-STAD	Stomach	499	1880	1397	485,576	4196	60,483	2354	487	472	18,090	17,253
TCGA-LGG	Lower Grade Glioma	533	1880	1287	485,576	4193	60,483	1560	487	472	18,090	17,253
TCGA-COAD	Colon	539	1880	1460	485,576	4671	60,483	1931	487	472	18,090	17,253
TCGA-UCEC	Endometrioid	588	1880	1414	485,576	4424	60,483	2849	487	472	18,090	17,253
TCGA-HNSC	Head and Neck	611	1880	1428	485,576	4358	60,483	2059	487	472	18,090	17,253
TCGA-THCA	Thyroid	614	1880	1369	485,576	4160	60,483	1432	487	472	18,090	17,253
TCGA-PRAD	Prostate	623	1880	1334	485,576	4006	60,483	1635	487	472	18,090	17,253
TCGA-LAML	Acute Myeloid Leukemia	626	1880	1140	485,576	4415	60,483	1032	487	472	18,090	17,253
TCGA-GBM	Glioblastoma	649	1880	1023	485,576	4076	60,483	1206	487	472	18,090	17,253
TCGA-LUAD	Lung Adenocarcinoma	728	1880	1360	485,576	4480	60,483	2562	487	472	18,090	17,253
TCGA-OV	Ovarian	731	1880	1430	485,576	4254	60,483	2116	487	472	18,090	17,253
TCGA-LUSC	Lung Squamous Cell Carcinoma	752	1880	1375	485,576	4302	60,483	2610	487	472	18,090	17,253
TCGA-KIRC	Kidney Clear Cell Carcinoma	979	1880	1333	485,576	4399	60,483	2274	487	472	18,090	17,253
TCGA-BRCA	Breast	1260	1880	1418	485,576	4195	60,483	3671	487	472	18,090	17,253

#### 4.5. Clinical Endpoints

To assess the performance of the SeNMo framework, we selected diagnostic and prognostic endpoints. The first end-point is OS, which is treated as a regression task. The second is the prediction of primary cancer type, formulated as a 33-class classification task. The third endpoint is TLS ratio prediction, also a regression task.

##### 4.5.1. Primary Cancer Type

Diagnosing primary cancer type based on biological and clinical features is critical for accurate treatment selection, improving patient outcomes, and enabling personalized therapies [35,36]. Since treatments and prognoses vary across cancer types, precise classification supports tailored interventions, follow-up care, and early recurrence detection. High classification accuracy enhances clinical decision-making, ultimately benefiting patient survival and quality of life. The distribution of patient samples across 33 cancer types is shown in Figure 1A.

##### 4.5.2. Overall Survival (OS)

Cancer prognosis through survival outcomes is a standard approach for biomarker discovery, patient stratification, and assessing therapeutic response [5]. Advances in statistical

survival models and deep learning have improved OS prediction by integrating molecular and clinical data [37,38]. In this study, we analyze clinical, demographic, and genomic factors to assess their correlation with patient survival, implementing OS prediction as a regression task in days. Survival data includes time-to-event records, accounting for right censoring when exact survival times are unknown. Figure 1B illustrates survival times since cancer diagnosis for the pan-cancer dataset. Each patient's outcome is characterized by two variables: a censoring indicator, also known as the vital status, and the observed time  $T = \min(T_s, T_\delta)$ , where  $T_s$  represents the true survival time and  $T_\delta$  is the censoring time,  $\{T_s \leq T_\delta\}$  [7]. The survival function, which describes the probability that a patient will survive beyond a specified time  $t$ , is given by:

$$F(t) = P\{T > t\}. \quad (3)$$

Additionally, the hazard function provides insight into the risk of an event occurring at a particular time, given survival up to that point. It represents the instantaneous rate of events (e.g., death) occurring at a specific time, conditional on having survived to that time. The hazard function  $h(t)$  is mathematically defined as the ratio of the probability of the event occurring in a short interval around  $t$  to the probability of surviving beyond  $t$ :

$$h(t) = \lim_{\Delta t \rightarrow 0} \frac{P(t \leq T < t + \Delta t \mid T \geq t)}{\Delta t}, \quad (4)$$

where  $h(t)$  is the hazard function at time  $t$ ,  $T$  is the survival time,  $P(t \leq T < t + \Delta t \mid T \geq t)$  is the conditional probability that the event occurs in the time interval  $[t, t + \Delta t)$  given that survival time is greater than or equal to  $t$ , and  $\Delta t$  represents an infinitesimally small time interval. Based on survival data, the hazard function describes the instantaneous risk of experiencing the event of interest at any given time. In our study, right-censoring was defined as censor  $\delta = 1$  in case of an event (e.g., death), and 0 otherwise.

#### 4.5.3. Tertiary Lymphoid Structures (TLS) Ratio

TLSs are immune cell aggregates resembling secondary lymphoid organs, forming in inflamed tissues, including cancers, and are associated with improved survival and immunotherapy response [39,40]. The TLS ratio (segmented TLS area/total tissue area) serves as a prognostic biomarker, influencing clinical decision-making. Automated TLS segmentation models have shown high accuracy across multiple cancers [39,40]. In this study, whole slide images of H&E and CD20-stained sections were analyzed using Visiopharm 2022.03. Visiopharm Tissuealign co-registered serial images, tumor and non-tumor regions were manually segmented, and TLSs were detected via thresholding, followed by manual review and feature extraction by an experienced image analysis technician under pathologist supervision. The tissue-level TLS ratio was calculated as the ratio of the segmented TLS area to the total tissue area. The initial sample count for data was  $N = 108$ . As shown in Figure 5a, out of the 108 patients, 7 had missing TLS labels and were excluded from the study.

#### 4.6. SeNMo Deep Learning Model

In scenarios involving hundreds or thousands of features with relatively few training samples, feedforward networks often face the risk of overfitting [5]. Unlike CNNs, weights in feedforward networks are shared, making them vulnerable to training instabilities caused by perturbations and regularization techniques such as stochastic gradient descent and dropout. CNNs, on the other hand, struggle to handle high-dimensional, low-sample data due to the spatial invariance assumption, fixed input size, and inefficiencies in managing multi-omics data sparsity. Transformer-based models are also suboptimal

for high-dimensional, low-sample data, as they rely heavily on attention mechanisms tailored for predicting sequential patterns, which fails when dealing with highly sparse molecular data. To address the challenges of overfitting and instability in high-dimensional, low-sample-size multi-omics data, we drew inspiration from self-normalizing networks introduced by Klambauer et al. [41]. Self-normalizing neural networks are particularly suited for high-dimensional datasets with limited samples, a characteristic that makes them highly relevant for multi-omics analysis. The SeNMo architecture is based on stacked layers of self-normalizing neural networks, as detailed below.

SeNMo comprises stacked blocks of self-normalizing neural network layers, where each block includes a linear unit, a Scaled Exponential Linear Unit (SELU) activation, and Alpha-Dropout. These components enable high-level abstract representations while keeping neuron activations close to zero mean and unit variance [41]. The linear unit is equivalent to a “fully connected” or MLP layer commonly used in traditional neural network architectures. Klambauer et al. demonstrated through the Banach fixed-point theorem that activations with close proximity to zero mean and unit variance, propagating through numerous network layers, will ultimately converge to zero mean and unit variance [41]. SELU activations, an alternative to traditional rectified linear unit activations, offer a self-normalizing effect, ensuring activations converge to zero mean and unit variance regardless of the input distribution. The SELU activation function is expressed mathematically as:

$$\text{SELU}(x) = \lambda \begin{cases} x & \text{if } x > 0 \\ \alpha(e^x - 1) & \text{if } x \leq 0, \end{cases} \quad (5)$$

where  $\lambda$  is a scaling factor (typically set to 1.05071) and  $\alpha$  is the negative scale factor (typically set to 1.6733).

Dropout, a regularization method that randomly sets a fraction of input units to zero during training, prevents overfitting. Alpha-Dropout, a modified version of traditional dropout, is designed to maintain the self-normalizing property of SELU activations. It applies a dropout mask during training, scaled to ensure the mean and variance of activations remain stable. The scaling factor is computed based on the dropout rate and the SELU parameters ( $\lambda$  and  $\alpha$ ). Alpha-Dropout is mathematically defined as:

$$\text{Alpha-dropout}(x) = \frac{x - \mu(x)}{\text{std}(x)} \times \text{mask} + \mu(x), \quad (6)$$

where  $x$  is the input activation,  $\mu(x)$ ,  $\text{std}(x)$  are the mean and standard deviation of the input activation, respectively, and  $\text{mask}$  is a binary mask generated with the specified dropout rate.

Together, SELU activations and Alpha-Dropout ensure that SeNMo blocks maintain stable mean and variance across network layers, facilitating more reliable training and better generalization performance. Additionally, these mechanisms help mitigate training instabilities related to vanishing or exploding gradients in feedforward networks. Our network architecture consists of seven fully connected hidden layers, each followed by SELU activation and Alpha-Dropout. The final fully connected layer is used to learn a latent representation of each sample, termed as the patient embedding  $\mathbf{x} \in \mathbb{R}^{48}$ .

#### 4.7. Training and Evaluation

##### 4.7.1. Data Splits

For the OS task, the pan-cancer data was randomly divided into the training-validation set (80%) and the hold-out test set (20%) for each cancer type. The pan-cancer training was carried out by combining the training-validation cohort of all 33 cancer types and

adopting the 10-fold cross-validation with the 80–20% division of samples. The training-validation cohort has 11,050 patients, each having  $\mathbb{R}^{80,697}$  features, comprising the six modalities mentioned earlier. For the evaluation/testing of the trained model, the inference data was created by combining the held-out test set from all 33 cancer types, resulting in 2754 patients. We tested the optimal hyperparameters of our trained model to train different combinations of the pan-cancer data modalities. We call these 1-modal, 3-modal (gene expression, DNA methylation, miRNA expression), 4-modal (3+protein expression), 5-modal (4+DNA mutation), and 6-modal (all modalities) cohorts. Although our initial model was trained on all 6 modalities, these experiments aim to see how the model performs on each of these pan-cancer cohorts where one or more of the data modalities is missing.

#### 4.7.2. Evaluation

We evaluate SeNMo's performance with the quantitative and statistical metrics common for survival outcome prediction and classification. For survival analysis, we evaluated the model using the C-index. For the primary cancer type classification, we generate the classification report comprising average accuracy, average precision, recall, F1-score, confusion matrix, and scatter plot. For the TLS Ratio, we employed Huber Loss. We utilized the log-rank test to determine if the survival predictions were statistically significantly different. For details on each evaluation metric, see Appendix B.

#### 4.8. Study Design

An overview of the various simulations conducted to evaluate the capabilities of the SeNMo model across different learning regimes, tasks, and datasets is shown in Figure 1E. The simulations included multiple learning regimes, each designed to assess the model's adaptability, generalizability, and robustness on diagnostic and prognostic tasks. The baseline model was initially trained on the TCGA dataset comprising 33 different cancer types for OS prediction. The subsequent learning regimes explored different data variations and tasks, which we call out-of-distribution simulations because the model had not encountered such data/task in baseline learning. These scenarios included OS prediction on both seen and unseen datasets, as well as tasks such as primary cancer type classification on seen data and TLS ratio prediction on unseen data.

## 5. Conclusions

In this study, we introduced SeNMo, a deep learning model specifically designed for multi-omics data analysis. SeNMo offers an end-to-end framework that unifies prognostic, diagnostic, and immune micro-environment modeling within a single, modality-agnostic network. The results highlight that self-normalizing architectures alleviate the optimization challenges posed by high-dimensional, sparse multi-omics data, enabling reliable performance even in incomplete or shifted domains. By making SeNMo and its derived patient embeddings publicly available, we aim to facilitate further research and innovation in personalized cancer care, underscoring the transformative potential of multi-omics approaches in the fight against cancer.

**Author Contributions:** A.W., A.T., S.A., H.F., M.B.S., P.A.S., M.N. and G.R. conceived the idea, A.W., A.T., S.A., A.M., M.B.S., P.A.S. and G.R. are responsible for conceiving, writing and evaluating the implementation and simulations in Python, G.R., P.A.S., M.B.S., M.N. and J.O.J. verified the concept, implementation, methodology, and results. A.W., A.T., S.A. and A.M. wrote the initial draft manuscript. All authors have read and agreed to the published version of the manuscript.

**Funding:** This work has been supported in part by the National Science Foundation awards 1903466, 2008690, 2234836, 2234468, NIH grant U01CA200464, grant from the State of Florida Bankhead Coley Research Program (21B12), in part by the Biostatistics and Bioinformatics Shared Resource

at the H. Lee Moffitt Cancer Center & Research Institute (P30-CA076292), and Huntsman Cancer Foundation and the National Cancer Institute of the National Institutes of Health under Award Number P30CA042014.

**Institutional Review Board Statement:** Ethical review and approval were not necessary for this study, as all data used were publicly available.

**Informed Consent Statement:** Patient consent was not necessary for this study, as all data used were publicly available and fully de-identified.

**Data Availability Statement:** The molecular data, overall survival information, and other phenotypes from the TCGA and corresponding labels are available from NIH Genomic Data Commons (<https://portal.gdc.cancer.gov/>, accessed on 22 July 2025). The gene expression, miRNA expression, and DNA Methylation data was obtained from UCSC XENA (<https://xena.ucsc.edu/>, accessed on 22 July 2025). The CPTAC-LSCC and Moffitt LSCC data are available at [14,15]. The codebase for the project is available at <https://github.com/lab-rasool/SeNMmo> accessed on 22 July 2025. The trained model checkpoints for the baseline SeNMmo model along with the sample embeddings for future use are available in two parts at <https://doi.org/10.5281/zenodo.14219799> (accessed on 22 July 2025) and <https://doi.org/10.5281/zenodo.14286190> (accessed on 22 July 2025).

**Conflicts of Interest:** The authors declare no conflicts of interest.

## Appendix A. Multi-Omic Data Modalities

Below is a brief description of each data modality considered in this study.

1. DNA methylation: DNA methylation is an epigenetic modification involving the addition of methyl groups to the DNA molecule, typically at cytosine bases adjacent to guanine, known as CpG sites [42]. This modification plays a crucial role in regulating gene expression without altering the DNA sequence [42]. In cancer, aberrant methylation can lead to the silencing or activation of genes, contributing to oncogenesis and tumor progression [43]. Analyzing methylation profiles across different cancer types helps identify risk and diagnostic markers, predict disease progression, and support personalized treatment strategies [43]. DNA methylation is quantified through beta values ranging from 0 to 1, with higher values indicating increased methylation [44]. The beta values for TCGA-GDC methylation data were obtained using the Illumina Human Methylation 450 platform, which provides detailed methylation profiling [45]. The dataset contains 485,576 unique cg and rs methylation sites across multiple tumor types [45].
2. Gene expression (RNAseq): Gene expression analysis through RNA sequencing (RNAseq) is a powerful modality in cancer research, providing insights into the transcriptomic landscape of tumors [46]. This technique quantifies the presence and quantity of RNA in a biological sample, giving a detailed view of transcriptional activity in a cell [46]. RNAseq helps identify genes that are upregulated or downregulated in cancer cells compared to normal cells, offering clues about oncogenic pathways and potential therapeutic targets [47]. TCGA-GDC gene expression data was obtained from RNAseq, utilizing High-throughput sequence Fragments Per Kilobase of transcript per Million mapped reads (HTseq-FPKM) for normalization [48]. This approach normalizes raw read counts by gene length and the number of mapped reads, with further processing involving incrementing the FPKM value by one followed by log transformation to stabilize variance and enhance statistical analysis [49]. The dataset includes 60,483 genes, with FPKM values indicating gene expression levels. Values above 1000 signify high expression, while values between 0.5 and 10 indicate low expression [48,50]. Importantly, TCGA-GDC uses annotation sources such as GENCODE or Ensembl, which catalog various gene types beyond just protein-coding

- ones, resulting in a comprehensive transcriptome dataset rather than a protein-coding gene-only dataset [18].
3. miRNA stem loop expression: miRNA stem-loop expression plays a pivotal role in understanding the regulatory mechanisms of miRNAs (microRNAs) in gene expression [51]. miRNAs are small, non-coding RNA molecules that function by binding to complementary sequences on target mRNA transcripts, leading to silencing [51]. The expression of miRNAs involves multiple steps to ensure specific targeting and effective modulation of gene expression, which is crucial for normal cellular function as well as pathological conditions like cancer [51]. miRNA expression values for TCGA-GDC were measured using stem-loop expression through Illumina, and values were log-transformed after the addition of one [52,53]. The data represents 1880 features across hsa-miRNA sites, with expression levels varying between high and low.
  4. Protein expression: Reverse Phase Protein Array (RPPA) is a laboratory technique similar to western blotting, used to quantify protein expression in tissue samples [54]. The method involves transferring antibodies onto nitrocellulose-coated slides to bind specific proteins, forming quantifiable spots via a DAB calorimetric reaction and tyramide dye deposition, analyzed using “SuperCurve Fitting” software [54,55]. RPPA effectively compares protein expression levels in tumor and benign samples, highlighting aberrant protein levels that define the molecular phenotypes of cancer [54,56]. RPPA data in TCGA was derived from profiling nearly 500 antibody-proteins for each patient and deposited in The Cancer Proteome Atlas portal [57]. Each dataset includes the antigen ID, peptide target ID, gene identifier that codes for the protein, and antigen expression levels. Protein expression levels were normalized through log transformation and median centering after being calculated by SuperCurve fitting software [58].
  5. DNA mutation: Analyzing DNA sequences involves identifying mutated regions compared to a reference genome, resulting in Variant Calling Format (VCF) files detailing these differences [59,60]. Aggregating VCF files to exclude low-quality variants and include only somatic mutations produces Mutation Annotation Format (MAF) files [61]. Unlike VCF files, which consider all reference transcripts, MAF files focus on the most affected references and include detailed characteristics and quantifiable scores that assess a mutation’s translational impact and clinical significance [61]. This information is critical because clinically significant mutations often result in major defects in protein structure, severely impacting downstream functions and contributing to cancer development [62]. The MAF files from TCGA-GDC contain 18,090 mutational characteristics [61].
  6. Clinical data: Clinical and patient-level data play a crucial role in cancer research, providing the foundation for identifying and characterizing patient cohorts [63]. Clinical data includes detailed patient information that is instrumental in understanding cancer epidemiology, evaluating treatment responses, and improving prognostic assessments [63]. Integrating clinical data with genomic and proteomic analyses can uncover relationships between molecular profiles and clinical manifestations of cancer [64]. Key clinical and patient-level covariates such as age, gender, race, and disease stage are particularly important in cancer research due to their impact on disease presentation, progression, and treatment efficacy [65–68]. Age is a critical factor as cancer incidence and type often vary significantly with age, influencing both the biological behavior of tumors and patient prognosis [65]. Gender also plays an important role, with certain cancers being gender-specific and others differing in occurrence and outcomes between genders due to biological, hormonal, and social factors [66]. Race

and ethnicity are linked to differences in cancer susceptibility, mortality rates, and treatment outcomes, which reflect underlying genetic, environmental, and socioeconomic factors [67]. Finally, cancer stage and histology at diagnosis are paramount for determining disease extent, guiding treatment decisions, and correlating directly with survival rates [68].

7. **Data Integration:** The individual modality features are integrated in an early fusion technique whereby the learning was done on the concatenated multi-omics data features. The model uses early, feature-level fusion: after standard preprocessing, each omics modality is represented by a fixed-length vector; these vectors are then horizontally concatenated to create a single patient-level feature vector that feeds the shared SeNMo learning network, as shown in Figure A1.

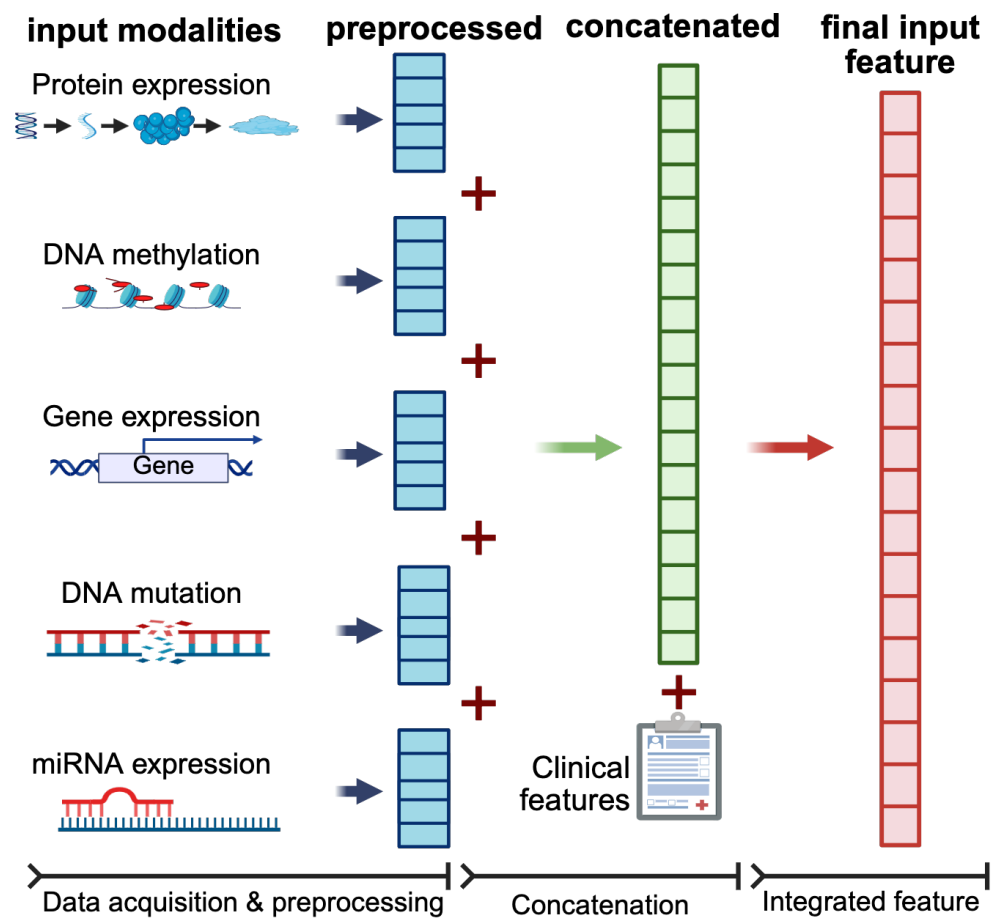


**Figure A1.** Early-fusion workflow used by SeNMo. Each omics data is first subjected to modality-specific preprocessing to yield a fixed-length feature vector (blue blocks). These preprocessed vectors are horizontally concatenated (red "+") to form a single multi-omic feature vector for each patient (green block). Structured clinical covariates are appended to this vector to form the final input feature (red block) for downstream modeling. This feature-level concatenation enables the model to preserve the modality-specific information.

## Appendix B. Model Evaluation

Below, we explain the loss, evaluation metrics, and statistical tests used in our experiments in detail.

1. **Loss Function:** The loss being used for backpropagation in the model is a combination of three components: Cox loss, cross-entropy loss, and regularization loss. This combined loss function aims to simultaneously optimize the model's ability to predict

survival outcomes (Cox loss), encourage model-simplicity or sparsity (regularization loss), and model the likelihood of cancer types (cross-entropy loss). The overall loss is a weighted sum of these three components, where each component is multiplied by a corresponding regularization hyperparameter ( $\lambda_c, \lambda_{ce}, \lambda_r$ ). This weighted sum allows for balancing the influence of each loss component on the optimization process. Mathematically, the overall loss can be expressed as:

$$L = \lambda_c L_{cox} + \lambda_{ce} L_{ce} + \lambda_r L_{reg}. \quad (A1)$$

- Cox proportional hazards loss ( $L_{cox}$ ): Cox loss is a measure of dissimilarity between the predicted hazard scores and the true event times in survival analysis. It is calculated using the Cox proportional hazards model and penalizes deviations between predicted and observed survival outcomes of all individuals who are at risk at time  $t_i$ , weighted by the censoring indicator [69]. The function takes a vector of survival times for each individual in the batch, the censoring status for each individual (1 if the event occurred, 0 if censored), and the predicted log hazard ratio for each individual from the neural network and returns the Cox loss for the batch, which is used to train the neural network via backpropagation. This backpropagation encourages the model to assign higher hazards to high-risk individuals and lower predicted hazards to censored individuals or those who experience the event later. Mathematically, the Cox loss is expressed as:

$$L_{cox} = -\frac{1}{N} \sum_{i=1}^N \left( \theta_i - \log \sum_{j=1}^N e^{\theta_j} \cdot R_{ij} \right) \cdot \delta_i, \quad (A2)$$

where  $N$  is the batch size (number of samples),  $\theta_i$  is the predicted hazard for sample  $i$ ,  $R_{ij}$  is the indicator function that equals 1 if the survival time of sample  $j$  is greater than or equal to the survival time of sample  $i$ , and 0 otherwise, and  $\delta_i$  is the censoring indicator for sample  $i$ , which equals 1 if the event is observed for sample  $i$  and 0 otherwise.

- Cross-entropy loss ( $L_{ce}$ ): The cross-entropy loss is a common loss function used for multi-class classification problems, particularly when each sample belongs to one of the  $C$  classes. When combined with a LogSoftmax layer, the function measures how well a model's predicted log probabilities match the true distribution across various classes. For a multi-class classification problem having  $C$  classes, the model's outputs (raw class scores or logits) are transformed into log probabilities using a LogSoftmax layer. The cross-entropy loss compares these log probabilities to the true distribution, which is usually represented in a one-hot encoded format. The loss is calculated by negating the log probability of the true class across all samples in a batch and then averaging these values. For the given output of LogSoftmax,  $\log(p_{n,c})$  for each class  $c$  in each sample  $n$ , the cross-entropy loss for a multi-class problem can be defined as:

$$L_{ce} = -\frac{1}{N} \sum_{n=1}^N \sum_{c=1}^C y_{n,c} \log(p_{n,c}), \quad (A3)$$

where  $N$  is the total number of samples,  $C$  are the total classes, and  $y_{n,c}$  is the target label for sample  $n$  and class  $c$ , typically 1 for the true class and 0 otherwise.

- Regularization loss ( $L_{reg}$ ): The regularization loss encourages the model's weights to remain small or sparse, thus preventing overfitting and improving

generalization. We used  $L1$  regularization to the SeNMo’s parameters, which penalizes the absolute values of the weights.

2. **Concordance Index (C-index):** The C-index is a key metric in survival analysis that evaluates a model’s predictive accuracy for time-to-event outcomes by measuring how well it ranks subjects based on predicted survival times [7]. It represents the probability that, in a randomly selected pair, the subject experiencing the event first has a higher predicted risk score. We used the *concordance\_index* function from Lifelines, which computes the fraction of correctly ordered event pairs among all comparable pairs [70]. The C-index ranges from 0 to 1, where 0.5 indicates random predictions, 1.0 perfect concordance, and 0.0 perfect anti-concordance [7]. Mathematically,

$$\text{C-Index} = \frac{(\text{Number of concordant pairs} + 0.5 \times \text{tied pairs})}{\text{Total number of evaluable pairs}}, \tag{A4}$$

$$\text{C-Index} = \Pr(\hat{S}_i < \hat{S}_j | T_i < T_j, \delta_i = 1), \tag{A5}$$

where concordant pairs are those where predicted survival times correctly align with observed outcomes, while tied pairs occur when predictions or survival times are identical. Total number of valuable pairs excludes cases with censoring or other exclusions. Predicted risks or survival probabilities for individuals  $i$  and  $j$  are  $\hat{S}_i$  and  $\hat{S}_j$ , respectively. A true event ordering ( $T_i < T_j$ ) means individual  $i$  experienced the event before  $j$ , and  $\delta_i = 1$  indicates that the event for  $i$  was observed (not censored).

3. **Cox log-rank function:** The Cox log-rank function calculates the  $p$ -value using the log-rank test based on predicted hazard scores, censor values, and true OS times. The log-rank test is a statistical method to compare the survival distributions of two groups or more groups, where the null hypothesis is that there is no difference between the groups. For the hazard ratio  $h_i(t)$  of group  $i$  at time  $t$ , the hypotheses are given by,

$$H_0 : h_1(t) = h_2(t) \tag{A6}$$

$$H_A : h_1(t) = \delta h_2(t), \delta \neq 1 \tag{A7}$$

The log-rank test statistic is computed by summing the squared differences between observed and expected events, divided by the expected events, across all time points. The resulting  $p$ -value indicates the significance of survival differences between groups. Under the null hypothesis, the test statistic follows a chi-squared distribution [70].

$$\chi^2 = \sum_{i=1}^N \frac{(O_i - E_i)^2}{E_i} \tag{A8}$$

where  $O_i$  is the observed number of events at time point  $i$  in the sample,  $E_i$  is the expected number of events at time point  $i$  under the null hypothesis, and  $N$  is the total number of observed time points.

4. **Huber Loss:** For TLS ratio prediction, we used Huber Loss, a loss function commonly used in regression tasks, known for combining the advantages of both the Mean Absolute Error (MAE) and the Mean Squared Error (MSE). It behaves differently based on the magnitude of the error; it is quadratic for small errors and linear for large errors. This characteristic makes it less sensitive to outliers than MSE and more sensitive to small errors than MAE. The Huber loss function is defined as follows:

$$L_n = \begin{cases} 0.5(y_n - \hat{y}_n)^2, & \text{if } |y_n - \hat{y}_n| \leq \delta, \\ \delta * (|y_n - \hat{y}_n| - 0.5 * \delta), & \text{otherwise.} \end{cases} \tag{A9}$$

where  $(y - \hat{y})$  represents the residual, which is the difference between the actual value and the predicted value, and  $\delta$  is a positive threshold parameter that determines the point at which the loss function transitions from quadratic to linear behavior [71].

5. Wilcoxon Signed-Rank Test: We used the Wilcoxon Signed-Rank test to evaluate the agreement between the manually annotated TLS ratio and the model's predictions. This non-parametric test considers both the magnitude and direction of differences in paired values. The null hypothesis assumes no significant difference between the distributions, with a two-sided  $p$ -value  $< 0.05$  indicating a statistically significant discrepancy.
6. Model Architecture: As illustrated in Figure A2, SeNMmo comprises stacked blocks of self-normalizing neural layers, where each block includes a linear unit, a Scaled Exponential Linear Unit (SELU) activation, and Alpha-Dropout. These components enable high-level abstract representations while keeping neuron activations close to zero mean and unit variance. The linear unit is equivalent to a "fully connected" or MLP layer commonly used in traditional neural network architectures.

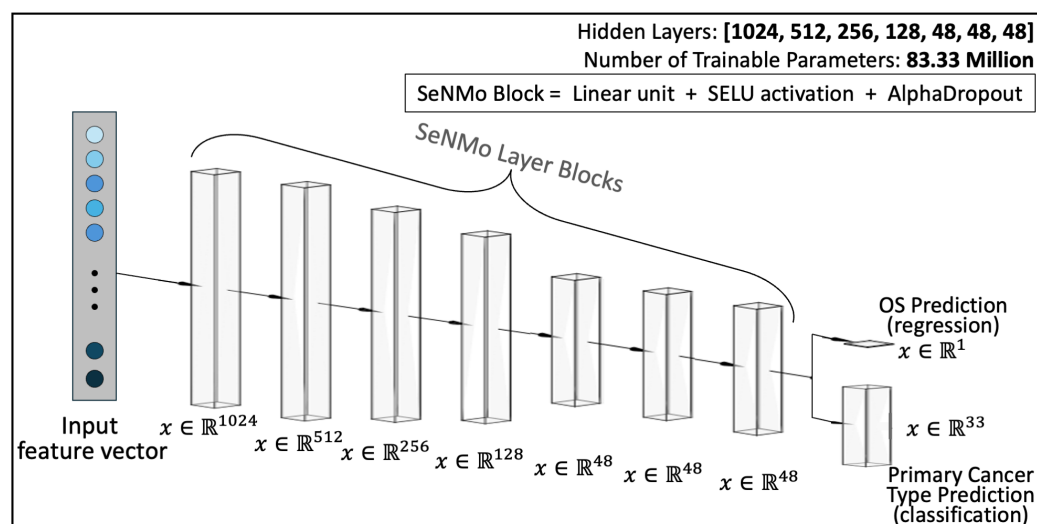


**Figure A2.** Architecture of the SeNMmo encoder network. There are seven hidden layers each comprising of a linear unit, SELU activation, and alpha-dropout. The trained model has 83.33 million parameters. The number of neurons in each hidden layer, input layer, and output layer are also depicted in the figure. The same model is used for regression and classification tasks.

### Appendix C. Hyperparameters Search

Hyperparameters are non-learnable parameters of a deep learning model and are crucial as they govern the learning process and model architecture. Hyperparameter tuning involves selecting the optimal combination of parameters that results in the best model performance. Common hyperparameters include learning rate and policy, batch size, number of epochs, weight decay, dropout type and probability, and architecture specifics such as the number of hidden layers and neurons in each layer. Methods for hyperparameter search range from grid search, where all possible combinations of parameters are evaluated, to random search, which randomly samples parameter combinations within predefined bounds. More sophisticated techniques like Bayesian optimization or using automated machine learning (AutoML) tools can dynamically adjust parameters based on previous results to find the best solutions more efficiently. We employed the weights and biases [72] utility to carry out random and Bayesian methods of hyperparameters search. The list of hyperparameters we searched for training is given in Table A1. For model training, we conducted around 400 simulations to find the current hyperparameters. To further verify the performance of our model, we evaluated the model with off-the-shelf datasets

CPTAC-LSCC [14] and Moffitt’s LSCC [15]. The plot for these simulations is given in Figure A3.

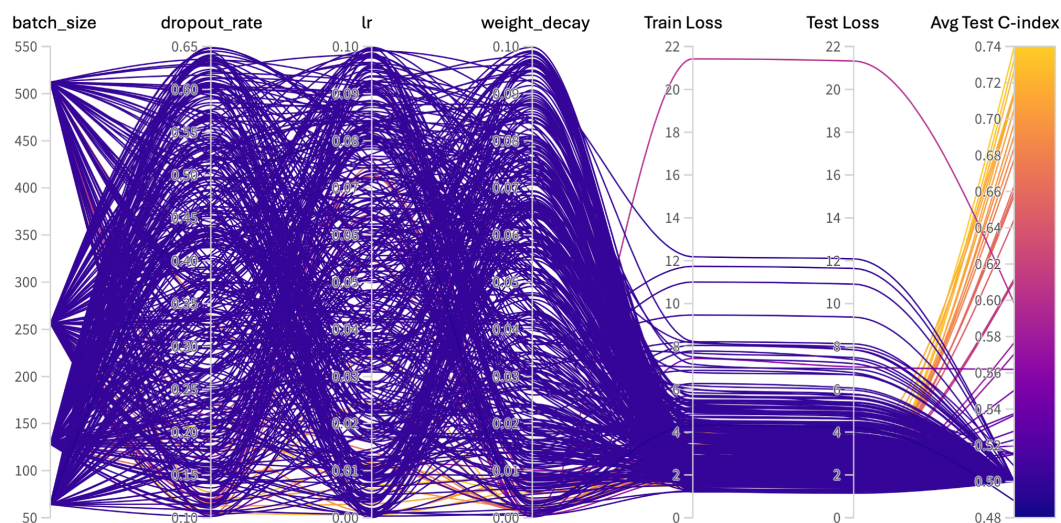


**Figure A3.** Hyperparameters search for training the SeNMo model on Pan-cancer multiomics data. The goal here was to maximize the validation C-Index.

**Table A1.** Hyperparameters search for training.

Hyperparams	Training (Range)
Learning Rate	$[1 \times 10^{-6}, 1 \times 10^{-1}]$
Weight Decay	$[1 \times 10^{-6}, 1 \times 10^{-1}]$
Dropout	[0.1, 0.65]
Batch Size	[64, 128, 256, 512]
Epochs	[50, 100]
Hidden Layers	[1, 2, 3, 4, 5, 6, 7, 8, 9]
Hidden Neurons	[2048, 1024, 512, 256, 128, 48, 32]
Optimizer	[adam, sgd, rmsprop, adamw]
Learning Rate Policy	[linear, exp, step, plateau, cosine]

## Appendix D. Frameworks, Compute Resources, and Wall-Clock Times

We trained the SeNMo model using the Moffitt Cancer Center’s HPC machine using one Tesla V100 32GB GPU running Ubuntu 22.04.4 and CUDA 12.2. The entire code was developed in Python and PyTorch frameworks. The software frameworks and corresponding packages used in our codebase are given in Table A2. Training time for our current 83.33 Million parameter SeNMo encoder is approximately 11 h. We conducted the hyperparameters search of the pan-cancer model for approximately 20 days using multiple GPUs in parallel. Fine-tuning the trained model on a given dataset having of around 150 patients takes approximately 15 min.

**Table A2.** Frameworks and packages used in our codebase.

	Package Name	Version
Operating systems	Ubuntu	20.04.4
Programming languages	Python	3.10.13
Deep learning framework	Pytorch torchvision	2.2.0 0.17.0
Miscellaneous	feature-engine	1.6.2
	imbalanced-learn	0.12.0
	scipy	1.12.0
	scikit-learn	1.4.0
	numpy	1.26.3
	PyYaml	6.0.1
	jupyter	1.0.0
	pandas	2.2.0
	pickle5	0.0.11
	protobuf	4.25.2
wandb	0.16.3	

### Appendix E. Additional Results

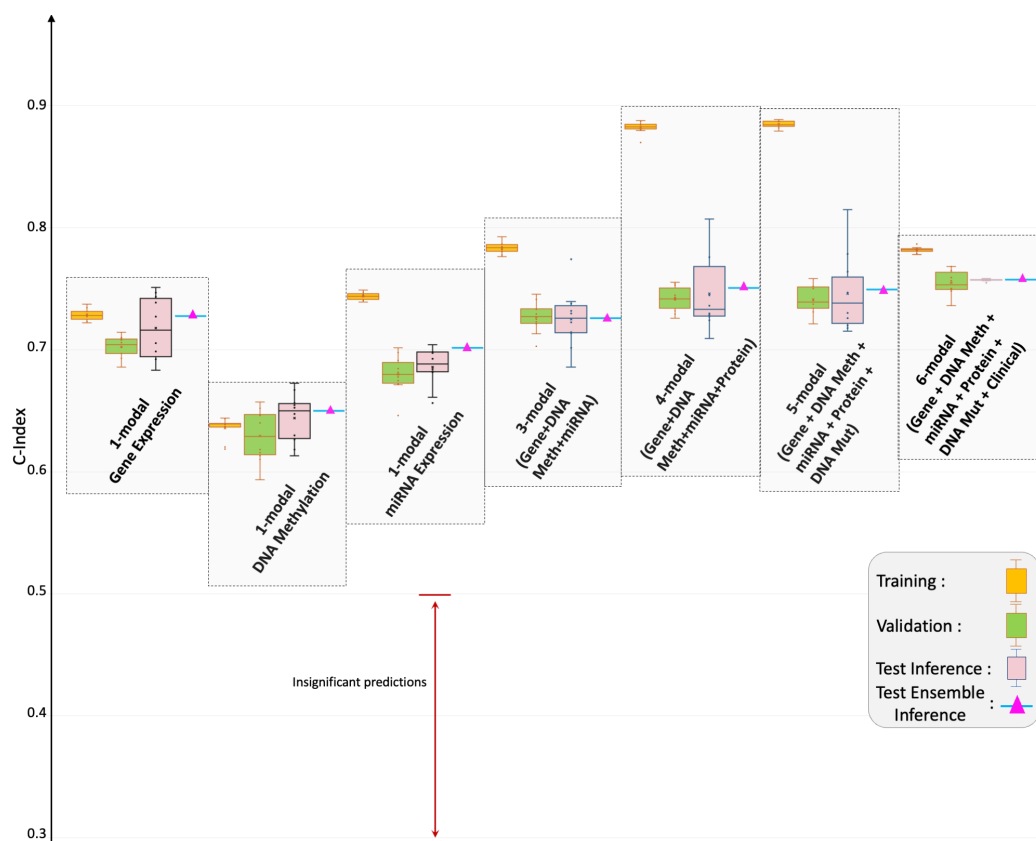


**Figure A4.** Pan-cancer C-Index results for OS prediction. The SeNMo model was trained and evaluated using different combinations of data modalities. Training and validation were carried out on 80% of the total data, whereas inference was done on the 20% held-out test set. As the number of modalities increased in the pan-cancer data, the model’s performance improved, as depicted by the upward trend of C-Index. All the results shown here are statistically significant, i.e.,  $p < 0.05$ .

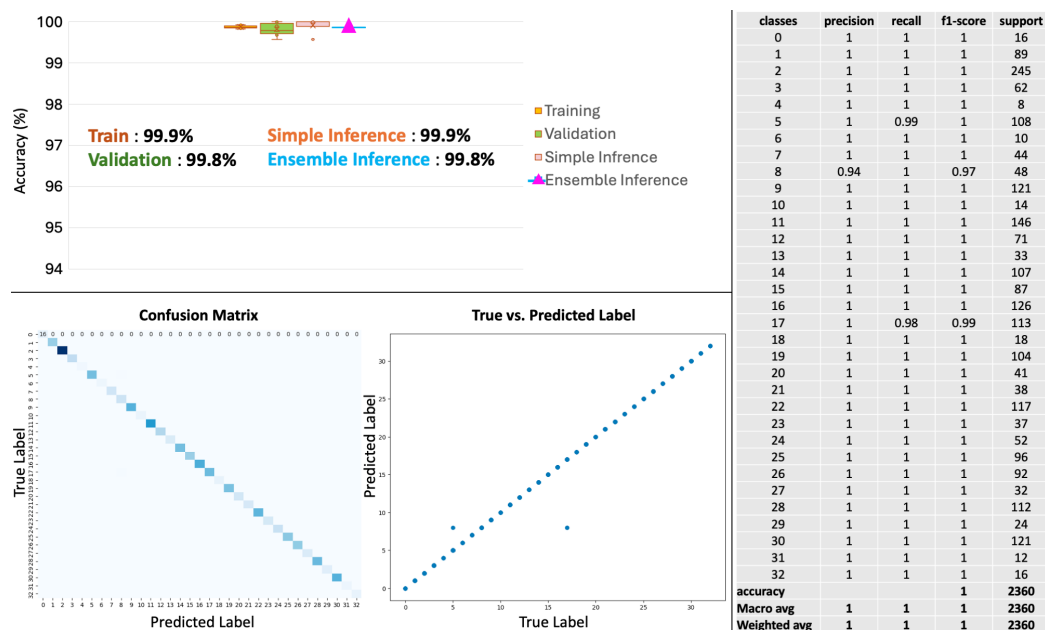


**Figure A5.** Pan-cancer primary cancer type prediction results. The model’s accuracy across training, validation, and inference stages is near-perfect (top left panel). Confusion matrix (bottom left) shows minimal misclassifications, while the scatter plot (bottom middle) shows the alignment of predicted versus true labels. The classification report (right panel) shows high precision, recall, and f1-scores in the 33 cancers type-identification.

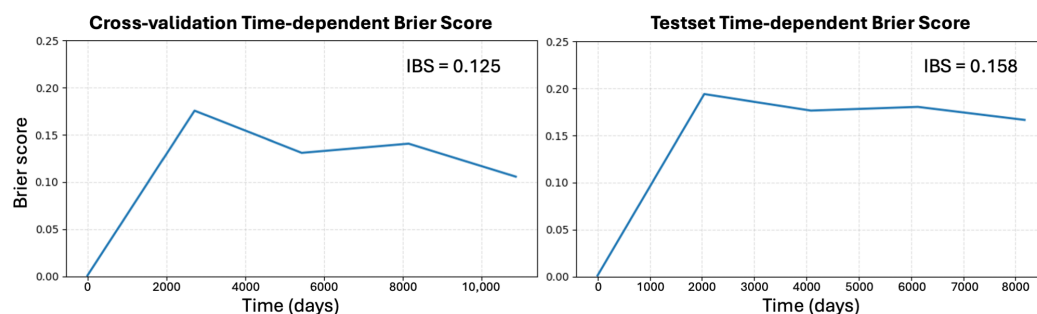


**Figure A6.** Time-dependent calibration of SeNMo. Left: mean Brier score  $BS(t)$  for cross-validation on the TCGA pan-cancer training data; right:  $BS(t)$  for the completely held-out pan-cancer test cohort. Survival probabilities were obtained from SeNMo’s log-partial hazards via the Breslow baseline, and  $BS(t)$  was computed with inverse-probability-of-censoring weights at equally spaced time points spanning the 10th–90th percentiles of follow-up. The integrated Brier score (IBS) summarizes each curve: 0.125 for cross-validation and 0.158 for the held-out test set. Both values lie well below the non-informative reference of 0.25, indicating that SeNMo’s predicted survival probabilities remain well-calibrated on unseen data despite a modest optimism gap expected from internal resampling. Lower  $BS(t)$  and IBS denote better combined discrimination and calibration.

## References

1. Harriott, N.C.; Chimenti, M.S.; Bonde, G.; Ryan, A.L. MixOmics Integration of Biological Datasets Identifies Highly Correlated Variables of COVID-19 Severity. *Int. J. Mol. Sci.* **2025**, *26*, 4743. [[CrossRef](#)]
2. Wang, J.; Wang, L.; Liu, Y.; Li, X.; Ma, J.; Li, M.; Zhu, Y. Comprehensive Evaluation of Multi-Omics Clustering Algorithms for Cancer Molecular Subtyping. *Int. J. Mol. Sci.* **2025**, *26*, 963. [[CrossRef](#)]
3. Tripathi, A.; Waqas, A.; Venkatesan, K.; Yilmaz, Y.; Rasool, G. Building Flexible, Scalable, and Machine Learning-ready Multimodal Oncology Datasets. *Sensors* **2024**, *24*, 1634. [[CrossRef](#)] [[PubMed](#)]
4. Tripathi, A.; Waqas, A.; Yilmaz, Y.; Rasool, G. HoneyBee: A Scalable Modular Framework for Creating Multimodal Oncology Datasets with Foundational Embedding Models. *arXiv* **2024**, arXiv:2405.07460. [[CrossRef](#)]

5. Chen, R.J.; Lu, M.Y.; Wang, J.; Williamson, D.F.; Rodig, S.J.; Lindeman, N.I.; Mahmood, F. Pathomic fusion: An integrated framework for fusing histopathology and genomic features for cancer diagnosis and prognosis. *IEEE Trans. Med. Imaging* **2020**, *41*, 757–770. [[CrossRef](#)]
6. Li, Z.; Jiang, Y.; Lu, M.; Li, R.; Xia, Y. Survival prediction via hierarchical multimodal co-attention transformer: A computational histology-radiology solution. *IEEE Trans. Med. Imaging* **2023**, *42*, 2678–2689. [[CrossRef](#)]
7. Zhao, Z.; Zabolos, J.; Zucknick, M.; Aittokallio, T. Tutorial on survival modeling with applications to omics data. *Bioinformatics* **2024**, *40*, btac132. [[CrossRef](#)]
8. Nikolaou, N.; Salazar, D.; RaviPrakash, H.; Goncalves, M.; Mulla, R.; Burlutskiy, N.; Markuzon, N.; Jacob, E. Quantifying the advantage of multimodal data fusion for survival prediction in cancer patients. *bioRxiv* **2024**. [[CrossRef](#)]
9. Liu, J.; Lichtenberg, T.; Hoadley, K.A.; Poisson, L.M.; Lazar, A.J.; Cherniack, A.D.; Kovatich, A.J.; Benz, C.C.; Levine, D.A.; Lee, A.V.; et al. An integrated TCGA pan-cancer clinical data resource to drive high-quality survival outcome analytics. *Cell* **2018**, *173*, 400–416. [[CrossRef](#)]
10. Pateras, J.; Lodi, M.; Rana, P.; Ghosh, P. Heterogeneous Clustering of Multiomics Data for Breast Cancer Subgroup Classification and Detection. *Int. J. Mol. Sci.* **2025**, *26*, 1707. [[CrossRef](#)]
11. Ballard, J.L.; Wang, Z.; Li, W.; Shen, L.; Long, Q. Deep learning-based approaches for multi-omics data integration and analysis. *BioData Min.* **2024**, *17*, 38. [[CrossRef](#)]
12. Bagaev, A.; Kotlov, N.; Nomie, K.; Svekolkin, V.; Gafurov, A.; Isaeva, O.; Osokin, N.; Kozlov, I.; Frenkel, F.; Gancharova, O.; et al. Conserved pan-cancer microenvironment subtypes predict response to immunotherapy. *Cancer Cell* **2021**, *39*, 845–865. [[CrossRef](#)]
13. Liu, Z.; Wang, Y.; Vaidya, S.; Ruehle, F.; Halverson, J.; Soljačić, M.; Hou, T.Y.; Tegmark, M. Kan: Kolmogorov-arnold networks. *arXiv* **2024**, arXiv:2404.19756.
14. Satpathy, S.; Krug, K.; Beltran, P.M.J.; Savage, S.R.; Petralia, F.; Kumar-Sinha, C.; Dou, Y.; Reva, B.; Kane, M.H.; Avanesian, S.C.; et al. A proteogenomic portrait of lung squamous cell carcinoma. *Cell* **2021**, *184*, 4348–4371. [[CrossRef](#)] [[PubMed](#)]
15. Stewart, P.A.; Welsh, E.A.; Slebos, R.J.; Fang, B.; Izumi, V.; Chambers, M.; Zhang, G.; Cen, L.; Pettersson, F.; Zhang, Y.; et al. Proteogenomic landscape of squamous cell lung cancer. *Nat. Commun.* **2019**, *10*, 3578. [[CrossRef](#)] [[PubMed](#)]
16. Law, C.W.; Chen, Y.; Shi, W.; Smyth, G.K. voom: Precision weights unlock linear model analysis tools for RNA-seq read counts. *Genome Biol.* **2014**, *15*, R29. [[CrossRef](#)] [[PubMed](#)]
17. Love, M.I.; Huber, W.; Anders, S. Moderated estimation of fold change and dispersion for RNA-seq data with DESeq2. *Genome Biol.* **2014**, *15*, 550. [[CrossRef](#)]
18. Weinstein, J.N.; Collisson, E.A.; Mills, G.B.; Shaw, K.R.; Ozenberger, B.A.; Ellrott, K.; Shmulevich, I.; Sander, C.; Stuart, J.M. The cancer genome atlas pan-cancer analysis project. *Nat. Genet.* **2013**, *45*, 1113–1120. [[CrossRef](#)]
19. Goldman, M.; Craft, B.; Hastie, M.; Repečka, K.; McDade, F.; Kamath, A.; Banerjee, A.; Luo, Y.; Rogers, D.; Brooks, A.N.; et al. Visualizing and interpreting cancer genomics data via the Xena platform. *Nat. Biotechnol.* **2020**, *38*, 675–678. [[CrossRef](#)]
20. Sarhadi, V.K.; Armengol, G. Molecular biomarkers in cancer. *Biomolecules* **2022**, *12*, 1021. [[CrossRef](#)]
21. Li, Y.; Porta-Pardo, E.; Tokheim, C.; Bailey, M.H.; Yaron, T.M.; Stathias, V.; Geffen, Y.; Imbach, K.J.; Cao, S.; Anand, S.; et al. Pan-cancer proteogenomics connects oncogenic drivers to functional states. *Cell* **2023**, *186*, 3921–3944. [[CrossRef](#)]
22. Chen, F.; Wendl, M.C.; Wyczalkowski, M.A.; Bailey, M.H.; Li, Y.; Ding, L. Moving pan-cancer studies from basic research toward the clinic. *Nat. Cancer* **2021**, *2*, 879–890. [[CrossRef](#)]
23. Liao, J.; Chin, K.V. Logistic regression for disease classification using microarray data: Model selection in a large p and small n case. *Bioinformatics* **2007**, *23*, 1945–1951. [[CrossRef](#)]
24. Galli, S. Feature-engine: A Python package for feature engineering for machine learning. *J. Open Source Softw.* **2021**, *6*, 3642. [[CrossRef](#)]
25. Bommert, A.; Welchowski, T.; Schmid, M.; Rahnenführer, J. Benchmark of filter methods for feature selection in high-dimensional gene expression survival data. *Briefings Bioinform.* **2022**, *23*, bbab354. [[CrossRef](#)] [[PubMed](#)]
26. Pedregosa, F.; Varoquaux, G.; Gramfort, A.; Michel, V.; Thirion, B.; Grisel, O.; Blondel, M.; Prettenhofer, P.; Weiss, R.; Dubourg, V.; et al. Scikit-learn: Machine Learning in Python. *J. Mach. Learn. Res.* **2011**, *12*, 2825–2830.
27. Sha, Y.; Phan, J.H.; Wang, M.D. Effect of low-expression gene filtering on detection of differentially expressed genes in RNA-seq data. In Proceedings of the 2015 37th Annual International Conference of the IEEE Engineering in Medicine and Biology Society (EMBC), Milan, Italy, 25–29 August 2015; pp. 6461–6464.
28. Deyneko, I.; Mustafaev, O.; Tyurin, A.; Zhukova, K.; Varzari, A.; Goldenkova-Pavlova, I. Modeling and cleaning RNA-seq data significantly improve detection of differentially expressed genes. *BMC Bioinform.* **2022**, *23*, 488. [[CrossRef](#)]
29. Zehetmayer, S.; Posch, M.; Graf, A. Impact of adaptive filtering on power and false discovery rate in RNA-seq experiments. *BMC Bioinform.* **2022**, *23*, 388. [[CrossRef](#)]
30. Gonzalez, T.L.; Sun, T.; Koepfel, A.F.; Lee, B.; Wang, E.T.; Farber, C.R.; Rich, S.S.; Sundheimer, L.W.; Buttle, R.A.; Chen, Y.D.I.; et al. Sex differences in the late first trimester human placenta transcriptome. *Biol. Sex Differ.* **2018**, *9*, 4. [[CrossRef](#)]

31. Zhu, Z.; Gregg, K.; Zhou, W. iRGvalid: A Robust in silico Method for Optimal Reference Gene Validation. *Front. Genet.* **2021**, *12*, 716653. [CrossRef]
32. Anggraeny, F.T.; Purbasari, I.Y.; Munir, M.S.; Muttaqin, F.; Mandiyarta, E.P.; Akbar, F.A. Analysis of Simple Data Imputation in Disease Dataset. In Proceedings of the International Conference on Science and Technology (ICST 2018), Bali, Indonesia, 18–19 December 2018; Atlantis Press: Dordrecht, The Netherlands, 2018; pp. 471–475.
33. Ulriksborg, T.R. Imputation of Missing Time Series Values Using Statistical and Mathematical Strategies. Master's Thesis, Department of Informatics, University of Oslo, Oslo, Norway, 2022.
34. Yi, J.; Lee, J.; Kim, K.J.; Hwang, S.J.; Yang, E. Why not to use zero imputation? Correcting sparsity bias in training neural networks. *arXiv* **2019**, arXiv:1906.00150.
35. Tanvir, R.B.; Islam, M.M.; Sobhan, M.; Luo, D.; Mondal, A.M. MOGAT: A multi-omics integration framework using graph attention networks for cancer subtype prediction. *Int. J. Mol. Sci.* **2024**, *25*, 2788. [CrossRef]
36. Miller, K.D.; Nogueira, L.; Mariotto, A.B.; Rowland, J.H.; Yabroff, K.R.; Alfano, C.M.; Jemal, A.; Kramer, J.L.; Siegel, R.L. Cancer treatment and survivorship statistics, 2019. *CA A Cancer J. Clin.* **2019**, *69*, 363–385. [CrossRef]
37. Jaksik, R.; Szumala, K.; Dinh, K.N.; Śmieja, J. Multiomics-based feature extraction and selection for the prediction of lung cancer survival. *Int. J. Mol. Sci.* **2024**, *25*, 3661. [CrossRef]
38. Carreras, J.; Roncador, G.; Hamoudi, R. Artificial intelligence predicted overall survival and classified mature B-cell neoplasms based on immuno-oncology and immune checkpoint panels. *Cancers* **2022**, *14*, 5318. [CrossRef]
39. van Rijthoven, M.; Obahor, S.; Pagliarulo, F.; van den Broek, M.; Schraml, P.; Moch, H.; van der Laak, J.; Ciompi, F.; Silina, K. Multi-resolution deep learning characterizes tertiary lymphoid structures and their prognostic relevance in solid tumors. *Commun. Med.* **2024**, *4*, 5. [CrossRef]
40. Chen, Z.; Wang, X.; Jin, Z.; Li, B.; Jiang, D.; Wang, Y.; Jiang, M.; Zhang, D.; Yuan, P.; Zhao, Y.; et al. Deep learning on tertiary lymphoid structures in hematoxylin-eosin predicts cancer prognosis and immunotherapy response. *NPJ Precis. Oncol.* **2024**, *8*, 73. [CrossRef] [PubMed]
41. Klambauer, G.; Unterthiner, T.; Mayr, A.; Hochreiter, S. Self-normalizing neural networks. *Adv. Neural Inf. Process. Syst.* **2017**, *30*. Available online: [https://proceedings.neurips.cc/paper\\_files/paper/2017/file/5d44ee6f2c3f71b73125876103c8f6c4-Paper.pdf](https://proceedings.neurips.cc/paper_files/paper/2017/file/5d44ee6f2c3f71b73125876103c8f6c4-Paper.pdf) (accessed on 22 July 2025).
42. Loyfer, N.; Magenheimer, J.; Peretz, A.; Cann, G.; Bredno, J.; Klochendler, A.; Fox-Fisher, I.; Shabi-Porat, S.; Hecht, M.; Pelet, T.; et al. A DNA methylation atlas of normal human cell types. *Nature* **2023**, *613*, 355–364. [CrossRef] [PubMed]
43. Lakshminarasimhan, R.; Liang, G. The role of DNA methylation in cancer. In *DNA Methyltransferases-Role and Function. Advances in Experimental Medicine and Biology*; Springer: Cham, Switzerland, 2016; Volume 945, pp. 151–172.
44. Du, P.; Zhang, X.; Huang, C.C.; Jafari, N.; Kibbe, W.A.; Hou, L.; Lin, S.M. Comparison of Beta-value and M-value methods for quantifying methylation levels by microarray analysis. *BMC Bioinform.* **2010**, *11*, 587. [CrossRef]
45. Wang, Z.; Wu, X.; Wang, Y. A framework for analyzing DNA methylation data from Illumina Infinium HumanMethylation450 BeadChip. *BMC Bioinform.* **2018**, *19*, 15–22. [CrossRef]
46. Corchete, L.A.; Rojas, E.A.; Alonso-López, D.; De Las Rivas, J.; Gutiérrez, N.C.; Burguillo, F.J. Systematic comparison and assessment of RNA-seq procedures for gene expression quantitative analysis. *Sci. Rep.* **2020**, *10*, 19737. [CrossRef] [PubMed]
47. Hijazo-Pechero, S.; Alay, A.; Marín, R.; Vilariño, N.; Muñoz-Pinedo, C.; Villanueva, A.; Santamaría, D.; Nadal, E.; Solé, X. Gene expression profiling as a potential tool for precision oncology in non-small cell lung cancer. *Cancers* **2021**, *13*, 4734. [CrossRef] [PubMed]
48. Gonzalez, A.; Leon, D.A.; Perera, Y.; Perez, R. On the gene expression landscape of cancer. *PLoS ONE* **2023**, *18*, e0277786. [CrossRef]
49. Rau, A.; Flister, M.; Rui, H.; Auer, P.L. Exploring drivers of gene expression in the Cancer Genome Atlas. *Bioinformatics* **2019**, *35*, 62–68. [CrossRef] [PubMed]
50. Expression, G. Expression Atlas. 2024. Available online: <https://www.ebi.ac.uk> (accessed on 22 July 2025).
51. Peng, Y.; Croce, C.M. The role of MicroRNAs in human cancer. *Signal Transduct. Target. Ther.* **2016**, *1*, 15004. [CrossRef]
52. Chu, A.; Robertson, G.; Brooks, D.; Mungall, A.J.; Birol, I.; Coope, R.; Ma, Y.; Jones, S.; Marra, M.A. Large-scale profiling of microRNAs for the cancer genome atlas. *Nucleic Acids Res.* **2016**, *44*, e3. [CrossRef]
53. Lin, S.; Zhou, J.; Xiao, Y.; Neary, B.; Teng, Y.; Qiu, P. Integrative analysis of TCGA data identifies miRNAs as drug-specific survival biomarkers. *Sci. Rep.* **2022**, *12*, 6785. [CrossRef]
54. Documentation, G. Reverse Phase Protein Array. 2024. Available online: [https://docs.gdc.cancer.gov/Data/Bioinformatics\\_Pipelines/RPPA\\_intro/](https://docs.gdc.cancer.gov/Data/Bioinformatics_Pipelines/RPPA_intro/) (accessed on 22 July 2025).
55. Anderson, M. RPPA Description. 2024. Available online: [https://www.mdanderson.org/documents/core-facilities/FunctionalProteomicsRPPACoreFacility/RPPADescription\\_2016.pdf](https://www.mdanderson.org/documents/core-facilities/FunctionalProteomicsRPPACoreFacility/RPPADescription_2016.pdf) (accessed on 22 July 2025).
56. Chen, M.J.M.; Li, J.; Wang, Y.; Akbani, R.; Lu, Y.; Mills, G.B.; Liang, H. TCPA v3. 0: An integrative platform to explore the pan-cancer analysis of functional proteomic data. *Mol. Cell. Proteom.* **2019**, *18*, S15–S25. [CrossRef]

57. Li, J.; Lu, Y.; Akbani, R.; Ju, Z.; Roebuck, P.L.; Liu, W.; Yang, J.Y.; Broom, B.M.; Verhaak, R.G.; Kane, D.W.; et al. TCPA: A resource for cancer functional proteomics data. *Nat. Methods* **2013**, *10*, 1046–1047. [CrossRef]
58. Ju, Z.; Liu, W.; Roebuck, P.L.; Siwak, D.R.; Zhang, N.; Lu, Y.; Davies, M.A.; Akbani, R.; Weinstein, J.N.; Mills, G.B.; et al. Development of a robust classifier for quality control of reverse-phase protein arrays. *Bioinformatics* **2015**, *31*, 912–918. [CrossRef]
59. Commons, G.D. Mutation Annotation Format. 2024. Available online: [https://docs.gdc.cancer.gov/Encyclopedia/pages/Mutation\\_Annotation\\_Format/](https://docs.gdc.cancer.gov/Encyclopedia/pages/Mutation_Annotation_Format/) (accessed on 22 July 2025).
60. Commons, G.D. File Format—VCF. 2024. [https://docs.gdc.cancer.gov/Data/File\\_Formats/VCF\\_Format/](https://docs.gdc.cancer.gov/Data/File_Formats/VCF_Format/) (accessed on 22 July 2025).
61. Commons, G.D. File Format—MAF. 2024. Available online: [https://docs.gdc.cancer.gov/Data/File\\_Formats/MAF\\_Format/](https://docs.gdc.cancer.gov/Data/File_Formats/MAF_Format/) (accessed on 22 July 2025).
62. Mendiratta, G.; Ke, E.; Aziz, M.; Liarakos, D.; Tong, M.; Stites, E.C. Cancer gene mutation frequencies for the US population. *Nat. Commun.* **2021**, *12*, 5961. [CrossRef] [PubMed]
63. Morin, O.; Vallières, M.; Braunstein, S.; Ginart, J.B.; Upadhaya, T.; Woodruff, H.C.; Zwanenburg, A.; Chatterjee, A.; Villanueva-Meyer, J.E.; Valdes, G.; et al. An artificial intelligence framework integrating longitudinal electronic health records with real-world data enables continuous pan-cancer prognostication. *Nat. Cancer* **2021**, *2*, 709–722. [CrossRef] [PubMed]
64. Waqas, A.; Tripathi, A.; Ramachandran, R.P.; Stewart, P.; Rasool, G. Multimodal data integration for oncology in the era of deep neural networks: A review. *arXiv* **2023**, arXiv:2303.06471. [CrossRef] [PubMed]
65. Lewandowska, A.; Rudzki, G.; Lewandowski, T.; Strykowska-Gora, A.; Rudzki, S. Risk factors for the diagnosis of colorectal cancer. *Cancer Control* **2022**, *29*, 10732748211056692. [CrossRef]
66. Lopes-Ramos, C.M.; Quackenbush, J.; DeMeo, D.L. Genome-wide sex and gender differences in cancer. *Front. Oncol.* **2020**, *10*, 597788. [CrossRef]
67. Zavala, V.A.; Bracci, P.M.; Carethers, J.M.; Carvajal-Carmona, L.; Coggins, N.B.; Cruz-Correa, M.R.; Davis, M.; de Smith, A.J.; Dutil, J.; Figueiredo, J.C.; et al. Cancer health disparities in racial/ethnic minorities in the United States. *Br. J. Cancer* **2021**, *124*, 315–332. [CrossRef]
68. Yang, X.; Mu, D.; Peng, H.; Li, H.; Wang, Y.; Wang, P.; Wang, Y.; Han, S. Research and application of artificial intelligence based on electronic health records of patients with cancer: Systematic review. *JMIR Med. Inform.* **2022**, *10*, e33799. [CrossRef]
69. Ching, T. Cox Regression. 2024. Available online: <http://traversc.github.io/cox-nnet/docs/> (accessed on 22 July 2025).
70. Davidson-Pilon, C. Lifelines, Survival Analysis in Python. 2024. Available online: <https://doi.org/10.5281/zenodo.10456828> (accessed on 22 July 2025).
71. Documentation, P. HuberLoss. 2024. Available online: <https://pytorch.org/docs/stable/generated/torch.nn.HuberLoss.html> (accessed on 22 July 2025).
72. Biewald, L. Experiment Tracking with Weights and Biases. 2020. Available online: <https://www.wandb.com/> (accessed on 22 July 2025).

**Disclaimer/Publisher’s Note:** The statements, opinions and data contained in all publications are solely those of the individual author(s) and contributor(s) and not of MDPI and/or the editor(s). MDPI and/or the editor(s) disclaim responsibility for any injury to people or property resulting from any ideas, methods, instructions or products referred to in the content.